Nanoscale

ROYAL SOCIETY OF CHEMISTRY

PAPER

View Article Online
View Journal | View Issue

Check for updates

Cite this: *Nanoscale*, 2026, **18**, 9737

Integrating green chemistry into SPION development: a theranostic study on prostate cell models

Beatriz Morais,[a] Vital Filho,[a,b] Célia T. Sousa,[c] Fernanda Marques,[a] Sara Lacerda,[d] João Carlos Waerenborgh,[a,b,e] Bruno J. C. Vieira,[a,b,e] Teresa Pinheiro,[e,f] Rodica Mihaela Dinica,[g] Maria J. Carmezim,[h] Pedro M. P. Santos,[a,e] Sandra Même,[d] Dirk H. Ortgies,[i,j] Laura C. J. Pereira *[a,b,e] and Maria Paula Cabral Campello *[a,e]

Superparamagnetic iron oxide nanoparticles (SPIONs) represent versatile building blocks for multimodal theranostics. Here, Fe_3O_4@Au@Gd hybrid nanoplatforms synthesised *via* a green approach using *Nymphaea alba* leaf extract were systematically compared with their dextran-coated counterparts prepared by a conventional route. Structural and magnetic analyses confirmed comparable iron oxide crystallite sizes (~18 nm) for both methods, while PIXE quantification revealed substantially enhanced gadolinium (Gd) incorporation for the green-synthesised systems, reaching ~23% for the SP-LV-Au1–Gd formulation. The samples exhibit dual therapeutic activity through distinct, composition-dependent mechanisms. Radiosensitisation under ^{60}Co γ-irradiation is dominated by the gold (Au) shell and is associated with increased reactive oxygen species (ROS)-mediated cytotoxicity and ultrastructural damage in human prostate cancer (PC3) cells. In contrast, magnetic hyperthermia (MH) efficiency, quantified by the specific absorption rate, is markedly enhanced by Gd incorporation, which increases magnetic disorder and effective core size, thereby improving heat dissipation. MH-induced cytotoxicity is efficient and selective towards PC3 cells relative to normal RWPE-1 cells and occurs independently of ROS generation. Relaxometric measurements indicate that, despite substantial Gd inclusion, the strong transverse relaxivity of the iron oxide core yields predominantly T_2-weighted MRI contrast. These green-synthesised SPION–Au–Gd nanohybrids thus offer a sustainable, composition-tunable platform for integrated prostate cancer theranostics.

Received 9th January 2026,
Accepted 11th March 2026

DOI: 10.1039/d6nr00113k

rsc.li/nanoscale

Introduction

Superparamagnetic iron oxide nanoparticles (SPIONs) are increasingly recognised as multifunctional nanoplatforms that integrate diagnostic and therapeutic capabilities within a single construct. Their iron oxide cores—typically magnetite (Fe_3O_4) or maghemite (γ-Fe_2O_3)—provide high saturation magnetisation and superparamagnetic behaviour at physiological temperatures, enabling T_2-weighted MRI contrast enhancement, *in situ* heat generation under alternating magnetic fields (magnetic hyperthermia, MH), and modulation of tumour radiosensitivity.[1–4] Magnetic hyperthermia (MH) induces sub-

---

[a] *Centro de Ciências e Tecnologias Nucleares, C2TN, Instituto Superior Técnico, Universidade de Lisboa, E.N. 10, km 139, 7, 2695-066 Bobadela LRS, Portugal. E-mail: biatambara0504@gmail.com, Vital.filho@ctn.tecnico.ulisboa.pt, fmarujo@ctn.tecnico.ulisboa.pt, jcarlos@ctn.tecnico.ulisboa.pt, brunovieira@ctn.tecnico.ulisboa.pt, psantos@ctn.tecnico.ulisboa.pt, lpereira@ctn.tecnico.ulisboa.pt, pcampelo@ctn.tecnico.ulisboa.pt; Tel: +351219946233, +351219946259*

[b] *CeFEMA, Center of Physics, Engineering and Advanced Materials, Instituto Superior Técnico, Universidade de Lisboa, Av. Rovisco Pais, 1049-001 Lisboa, Portugal*

[c] *Departamento de Física Aplicada, Universidad Autonoma de Madrid, Avda. Francisco Tomás y Valiente 7, 28049 Madrid, Spain. E-mail: celia.tsousa@uam.es*

[d] *Centre de Biophysique Moléculaire, CNRS, UPR 4301, Université d'Orléans, Rue Charles Sadron, 45071 Orléans CEDEX 2, France. E-mail: sandra.meme@cnrs-orleans.fr, sara.lacerda@cnrs.fr*

[e] *Departamento de Engenharia e Ciências Nucleares, DECN, Instituto Superior Técnico, Universidade de Lisboa, E.N. 10, km 139, 7, 2695-066 Bobadela LRS, Portugal. E-mail: Teresa.pinheiro@tecnico.ulisboa.pt*

[f] *iBB-Institute for Bioengineering and Biosciences, Instituto Superior Técnico, Universidade de Lisboa, Av. Rovisco Pais, 1049-001 Lisboa, Portugal*

[g] *Faculty of Sciences and Environment, Department of Chemistry, Physics and Environment, "Dunărea de Jos" University of Galati, 111 Domnească Street, 800201 Galati, Romania. E-mail: rodica.dinica@ugal.ro*

[h] *ESTSetúbal, CDP2T, Instituto Politécnico de Setúbal, Setúbal, Portugal. E-mail: maria.carmezim@estsetubal.ips.pt*

[i] *Departamento de Física de Materiales, Universidad Autonoma de Madrid, Avda. Francisco Tomás y Valiente 7, 28049 Madrid, Spain. E-mail: dirk.ortgies@uam.es*

[j] *Nanomateriales for BioImaging Group, Instituto Ramón y Cajal de Investigación Sanitaria (IRYCIS), Ctra. De Colmenar Viejo km 9.300, 28034 Madrid, Spain*

lethal thermal stress that disrupts membrane integrity, denatures proteins, and triggers apoptosis, selectively ablating tumour cells while minimizing collateral damage to healthy tissues. MH can also synergistically enhance radiosensitivity by inhibiting DNA repair, promoting tumour reoxygenation, and increasing oxidative stress. These effects are particularly relevant because radiotherapy and hyperthermia target complementary tumour subpopulations: poorly perfused, hypoxic regions—typically resistant to ionizing radiation due to limited oxygen-derived radical formation—are highly susceptible to thermal stress. In parallel, S-phase cells (the DNA-replication phase), which exhibit relative radioresistance owing to active DNA synthesis and enhanced repair capacity, are inconsistently thermosensitive. By preferentially damaging these otherwise radioresistant S-phase cells, MH strengthens the overall tumour response to γ-radiation. Furthermore, growing evidence indicates that SPION-mediated heat and oxidative stress amplify radiation-induced DNA damage, highlighting the potential of these nanostructures as potent radiosensitisers capable of reducing required therapeutic doses.[5–8] In addition, using SPIONs as a nanoparticle platform enables simultaneous monitoring of tumour targeting *via* MRI, supporting their application in nanotheranostics.

The magnitude of these effects is strongly influenced by the core composition, oxidation state, particle size, and surface chemistry, which collectively also determine cytotoxicity and intracellular fate. For example, uncoated Fe_3O_4 has been shown to induce oxidative DNA damage in lung epithelial cells, whereas γ-Fe_2O_3 can stimulate reactive oxygen species (ROS) formation and trigger cell death in endothelial cells.[2,9–12] Importantly, insufficient surface stabilisation may promote partial oxidation or iron release over time, enhancing nonspecific ROS generation and compromising biocompatibility. To mitigate these issues, protective coatings such as polyethylene glycol (PEG) or dextran are commonly employed. However, commercial dextran- and carboxydextran-coated formulations (*e.g.*, Resovist®, Feridex®, and Sinerem®) exhibit limitations arising from weak polymer anchoring and susceptibility to aggregation in biological media, which can lead to coating detachment, reduced MRI performance, and unpredictable biodistribution.[13–16]

Refinements in surface engineering—through polymers, molecular ligands, or multifunctional hybrid shells—have been pivotal for enhancing nanoparticle stability, relaxivity, and therapeutic efficacy. In this context, green synthesis has emerged as a sustainable and versatile alternative, relying on plant extracts enriched in polyphenols, flavonoids, and other phytochemicals that act simultaneously as reducing and stabilising agents. SPIONs produced *via* these bio-mediated routes typically display controlled particle size, improved colloidal dispersion, and favourable biocompatibility, often accompanied by intrinsic redox activity with potential relevance for radiosensitization. Despite these advantages, batch-to-batch variability in phytochemical composition and the complex, dynamic nature of protein corona formation remain major challenges for reproducibility and targeted biomedical applications.[17–22] Gold-coated SPION hybrids (Fe_3O_4@Au) provide an advanced multifunctional platform. Gold shells stabilize iron oxide cores, prevent oxidation, reduce iron-mediated oxidative stress, and impart plasmonic and optical properties suitable for multimodal imaging and photothermal therapy (PTT). Although non-magnetic, Au serves as a robust scaffold for immobilizing Gd^{3+} binding *via* thiolated (–SH), dithiolated, and/or amine ligands—such as cysteamine or amine-terminated PEGs—enabling T_1/T_2 dual-contrast MRI. Both Au and Gd act as high-Z radiosensitizers—Au enhancing local energy deposition through photoelectric and Compton interactions, Gd contributing short-range Auger electron emission—synergizing with Fe-driven ROS generation and MH-induced inhibition of DNA repair.[23–26] These Fe_3O_4@Au@Gd hybrids therefore integrate MRI contrast enhancement, magnetic hyperthermia, PTT, and radiosensitization, while minimizing systemic Gd exposure and the associated risk of nephrogenic systemic fibrosis.[27,28] Preclinical studies report improved relaxivity, enhanced hyperthermia efficiency, and radiation dose amplification, illustrating their potential as multifunctional nanoplatforms for integrated cancer theranostics.[17,25]

Previous work from our group demonstrated that SPIONs synthesized by controlled-pH co-precipitation (MpH) exhibit superior magnetic behaviour and relaxometric performance compared to reduction–precipitation (MR/P) analogues when coated with dextran, gold-stabilized, and Gd-functionalized, for dual MRI contrast.[12] Herein, and building on these results, we introduce a sustainable MpH-based green synthesis route using *Nymphaea alba* leaf extract, which replaces dextran while preserving compatibility with one-pot gold coating, yielding the SP-LV nanoplatform.[29] We performed a systematic, quantitative comparison between the dextran-based and green SP-LV nanoplatforms across physicochemical, magnetic, imaging, and biological endpoints. For the green SP-LV system, we further systematically varied the SPION : extract : Au : Gd ratios, enabling assessment of how compositional tuning influences their performance (Scheme 1). This includes:

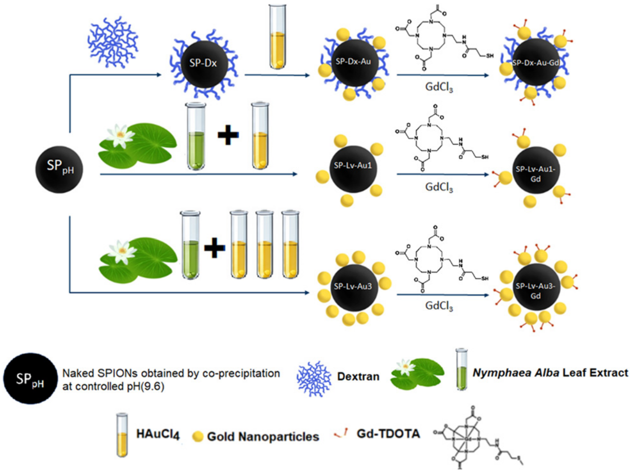

Scheme 1 Steps in the synthesis of the SPION nanoplatforms discussed in this article: SP-DX-Au–Gd, SP-LV-Au1–Gd, and SP-LV-Au3–Gd.

- Physicochemical properties: ultraviolet-visible (UV-Vis) spectroscopy, Fourier transform infrared (FTIR) spectroscopy, dynamic light scattering and zeta potential (DLS and ζ-potential) measurements, transmission electron microscopy (TEM) and proton-induced X-ray emission (PIXE).
- Magnetic and relaxometric performance: saturation magnetization ($M_{\text{Sat.}}$), hyperfine parameters (Mössbauer spectroscopy), and T_1/T_2 MRI contrast quantified by longitudinal and transverse relaxivities (r_1 and r_2).
- Magnetic hyperthermia (MH) efficiency: specific absorption rate (SAR) under clinically relevant AMF conditions, correlated with MH-induced cytotoxicity and determination of IC_{50} values in human cancer (PC3) and normal (RWPE-1) prostate cells.
- Radiosensitization efficacy: post-irradiation cell viability and quantification of radiation enhancement *via* dose-enhancement factors (DEF) following exposure to ^{60}Co γ-rays.
- Intracellular distribution and structural alterations: TEM analysis of nanoparticle-loaded and irradiated cells, assessing nanoparticle membrane perturbation, chromatin condensation, and ultrastructural damage.

By analysing these physicochemical, magnetic, imaging, thermal, and radiobiological endpoints in parallel, we aimed to establish a rigorous head-to-head comparison of MRI performance, MH-induced cytotoxicity, and γ-ray radiosensitization between the two systems, with the goal of contributing to the development of sustainable, biocompatible, and multifunctional nanoplatforms for multimodal cancer theranostics.

Results and discussion

Physicochemical characterization

In this work, we evaluate a new multifunctional, green-synthesized superparamagnetic iron oxide nanoparticle (SPION) platform using leaf extracts of *Nymphaea alba* from the Danube Delta. This bio-inspired nanoplatform is directly compared with a conventional dextran-coated SPION system, both originating from the same naked SPION core synthesized by co-precipitation at pH 9.6 (SPpH).[12] After primary coating, samples were gold-coated and further functionalized with gadolinium; the plant extract served as both a capping and reducing agent during gold deposition. We systematically varied the SPION : extract : Au : Gd ratios (Table 6, Materials and methods) and assessed their physicochemical and magnetic properties, as well as MRI performance (T_1/T_2 relaxivities and phantom imaging), cell studies in prostatic human cell lines (normal RWPE-1 and tumoral PC3) and evaluation of their therapeutic potential through γ-radiation and magnetic hyperthermia.

The absorption peaks in the UV-Vis spectrum for superparamagnetic iron oxide nanoparticles typically occur between 205–270 nm and 310–390 nm, and are consistently observed in all SPION samples.[12,30] For gold-coated SPIONs, pronounced peaks around 520–550 nm are visible in all spectra of the SP-LV nanoplatform, confirming the presence of gold nanoparticles.[12,31–33] In addition, the spectra display a peak near 270 nm and a broad band between 210 and 250 nm, attributable to the leaf extract coating, as supported by the matching absorption in the leaf extract spectrum.[33,34] These spectral features are consistent with those of the dextran-coated SPION nanoplatform, indicating that the coating type does not alter the fundamental optical profile of the SPION core (see Fig. S1). As previously observed for the dextran-coated SPpH nanoplatform, the infrared spectra of the SP-LV nanoplatform similarly show a progressive reduction in the intensity of characteristic bands from the coating material throughout successive functionalization steps (see Fig. S2). A broad peak between 3100 and 3600 cm^{-1} is observed and attributed to the stretching vibrations of hydroxyl (–OH) groups as well as the symmetric and asymmetric axial stretching of primary amines originally present in the leaf extract. Additionally, a band at 2900 cm^{-1} corresponds to C–H stretching, while bands between 1020 and 1250 cm^{-1} are associated with the N–H stretching and bending vibrations of the NH_2 amine group in the extract. Across all spectra, the band near 470–650 cm^{-1} is characteristic of metal–oxygen bonds and can be attributed to Fe–O stretching in iron oxides (Fe_2O_3 and Fe_3O_4).[12,34,35]

The iron, gold, and gadolinium content of the SPIONs of both nanoplatforms was determined by Particle-Induced X-ray Emission (PIXE), an ion beam analysis technique that uses MeV proton beams to ionize inner-shell electrons (Table S2). The subsequent relaxation of these electrons produces characteristic X-rays, enabling precise elemental identification and quantification. PIXE offers high sensitivity (detection limit in the mg kg^{-1} range) for elements with $Z > 13$ and, unlike ICP-OES, is performed on dry samples. Quantitative elemental analysis of the SPIONs by PIXE revealed clear differences in composition between the synthetic (SP-Dx) and green (SP-LV) platforms, with distinct Fe : Au ratios reflecting the synthesis strategy and precursor ratios. As expected, uncoated SPIONs (SP) exhibited the highest Fe content (≈89%). Coating with dextran and gold (SP-Dx-Au) reduced Fe to ≈42% and introduced ∼14% Au, giving an Fe : Au ratio close to 3 : 1. Incorporation of Gd (SP-Dx-Au–Gd) further lowered Fe to ∼34% and raised Au to ∼16%, with an Fe : Au ratio of ≈2.2 : 1, suggesting that Gd functionalization may promote a denser or differently distributed Au shell. In the SP-LV nanoplatform, the composition varied more strongly with synthesis conditions. SP-LV-Au3, prepared with higher Au precursor concentration, contained ∼40% Au and ∼19% Fe, yielding an inverted Fe : Au ratio of ≈1 : 2.1, consistent with a thick Au coating relative to the magnetic core. Conversely, SP-LV-Au1 showed ∼9% Au and ∼31% Fe (Fe : Au ≈ 3.3 : 1), more similar to the dextran-coated systems. Upon Gd functionalization, SP-LV-Au1–Gd exhibited the highest Fe : Au ratio (∼4.4 : 1) and the most efficient Gd incorporation (∼23%), compared with only ∼3.7% Gd in the dextran analogue (SP-Dx-Au–Gd). Overall, these results show that (i) Fe : Au ratios are strongly determined by the synthesis route and Au precursor amount; (ii) green synthesis with higher Au loading (SP-LV-Au3) yields gold-rich shells at the expense of Fe content, whereas lower Au loading (SP-LV-Au1) preserves more magnetic core; and (iii) Gd functionalization is more efficient in SP-LV-based systems, particularly SP-LV-Au1–Gd, which combines high Fe content with substantial Gd loading.

Powder X-ray diffraction (PXRD) patterns of all synthesized nanoplatforms exhibited a similar distribution of diffraction peaks at 2θ values of 18.27°, 30.09°, 35.42°, 43.05°, 53.39°, 56.94°, and 62.51°, corresponding to the (111), (220), (311), (400), (422), (511), and (440) crystal planes, consistent with both magnetite and maghemite phases (JCPDS files 19-629 and 39-1346, respectively). Additional peaks corresponding to the gold phase (JCPDS file 04-0784) were detected at approximately 38.31°, 44.46°, 64.67°, and 77.45°, corresponding to the (111), (200), (220), and (311) planes of the FCC structure, in agreement with values reported for these related nanoparticles.[12,36,37] The intensities of these gold peaks varied according to the gold content in each nanoplatform, reflecting the influence of Au loading on the diffraction patterns. The diffractograms in Fig. 1 clearly illustrate the influence of the SPION/gold ratio during synthesis. In SP-LV-Au3, the intensity of the (311) reflection associated with magnetite/maghemite is noticeably lower than that of the (111) reflection of gold, whereas in SP-LV-Au1 these peaks display comparable intensities. The PXRD patterns of SP-LV-Au3–Gd and SP-LV-Au1–Gd are shown in Fig. S3. It should also be noted that the apparent over-representation of gold reflections may result from the strong X-ray atomic scattering factor of gold nanoparticles. Given these limitations, PXRD alone cannot yield an accurate quantification of phase fractions; therefore, ^{57}Fe Mössbauer spectroscopy was employed to achieve a more precise phase analysis.[38–40]

The crystallite sizes of the SPIONs, estimated using the Debye–Scherrer equation, show an average core size of approximately 18 nm, consistent across the samples (Table 1). Notably, these values closely match those found for the corresponding dextran-coated SPIONs, *i.e.*, SP-Dx-Au and SP-Dx-Au–Gd, suggesting that both synthetic approaches to coating naked SPIONs yield similar magnetite crystallite sizes. Additionally, these crystallite sizes, which are below 20 nm, align well with reports on other SPIONs coated with dextran-based polymers and plant extracts.[12,41,42] The compositional differences revealed by PIXE, particularly in Au and Gd incorporation, are therefore not related to changes in the magnetic core size, but rather to the coating strategy; while the magnetic core size remains comparable across all nanoplatforms, Au and Gd incorporation is strongly dependent on the coating approach.

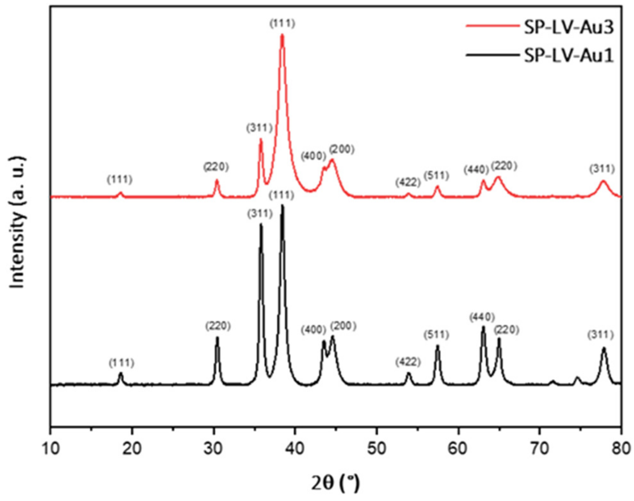

Fig. 1 Powder X-ray diffraction patterns of SP-LV-Au3 and SP-LV-Au1.

As an illustrative example, Fig. 2 displays the TEM images of SP-LV-Au1 (a) and SP-LV-Au3–Gd (b), acquired under bright-field conditions, while those of SP-LV-Au3 and SP-LV-Au1–Gd are shown in Fig. S4. The corresponding size distribution, standard deviation, and size dispersion (σ) values for both green (SP-LV) and dextran-coated (SP-Dx) nanoplatforms are summarized in Table 1 TEM analysis shows that, as observed for the SP-Dx nanoplatform, the SP-LV SPIONs, coated with gold using leaf extracts and further functionalized with gadolinium, are primarily quasi-spherical, although some irregular shapes are also present. The nanoparticles are well-dispersed, with average particle sizes consistent with those derived from PXRD analysis using the Scherrer equation (Table 1), suggesting that each SPION is a single crystal.

Slight variations between these values may be due to minor aggregation, as indicated by the relatively broad size dispersion. The average size of the nanoplatform with a higher gold-to-iron ratio (SP-LV-Au3) is approximately 18 nm, whereas the platform with a lower gold content (SP-LV-Au1) is around 14 nm. Following gadolinium functionalization, both samples exhibited an increase in size, reaching approximately 21 nm and 23 nm, respectively, consistent with observations reported for other gold/gadolinium-functionalized SPIONs.[12,42–44]

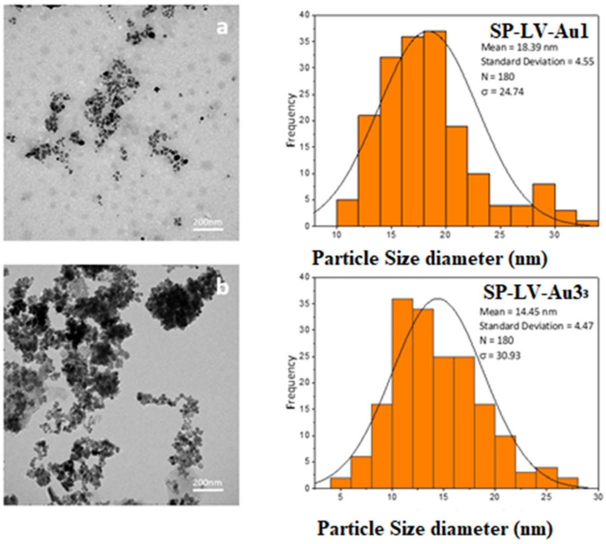

Fig. 2 Transmission electron microscopy images of (a) SP-LV-Au1, (b) SP-LV-Au3–Gd and respective histogram.

Together with the PXRD and elemental analysis data, the TEM results indicate that both dextran-coated (SP-Dx) and green-synthesized (SP-LV) nanoplatforms possess comparable magnetic core sizes, predominantly quasi-spherical shapes, and well-dispersed particles. However, variations in gold and gadolinium content, as reflected in PXRD peak intensities and PIXE measurements, highlight the strong influence of the coating strategy and precursor ratios on the shell composition and overall nanoplatform architecture.

Dynamic Light Scattering (DLS) was employed to determine the hydrodynamic diameter (D_H) of the SPIONs in aqueous suspension, assessing size-dependent fluctuations in scattered light associated with Brownian motion and providing information on their colloidal behaviour.[45,46] SP-LV-Au1–Gd and SP-LV-Au3–Gd exhibited D_H values of ∼29 nm and ∼45 nm, respectively, while the dextran-coated analogues showed similar trends (28–42 nm). Gadolinium functionalization caused slight changes in hydrodynamic size: an increase for SP-LV-Au3 and a decrease for SP-LV-Au1, consistent with rearrangements of the surface coatings (Table 1). Relatively high PDI values indicate heterogeneity, likely arising from particle size variations, irregular shapes, and partial aggregation in plant-extract-based SPIONs.[47,48] Consistent with the differing measurement principles, the hydrodynamic diameters were larger—typically about twice the TEM-derived core sizes—reflecting the contribution of coatings, solvation layers, and particle aggregation. TEM captures the physical size of individual particles in the solid state, distinguishing single particles from aggregates, whereas DLS measures the hydrodynamic diameter of particles in suspension, including coatings and solvation layers. Consequently, DLS averages over populations and is sensitive to aggregation, explaining the larger observed sizes.[12,33,47–49] All SPION formulations exhibited a net negative ζ-potential, with uncoated and dextran-coated SPIONs showing moderately negative values (≈−15 to −22 mV), whereas plant extract-coated SPIONs ranged more widely (≈−36 to −3 mV), likely reflecting the modulatory effect of Au and Gd content on surface charge (Table 1). Gadolinium functionalization induced a shift toward less negative potentials, particularly for SP-LV-Au1–Gd (≈−3.2 mV) and SP-LV-Au3–Gd (≈−6.9 mV). These shifts are consistent with previous reports showing that metal ions and coating composition can significantly modulate nanoparticle surface charge and colloidal stability. Smaller shifts in dextran-coated SPIONs (−21.5 to −16.7 mV) are consistent with lower Gd incorporation (∼10% *vs.* ∼25% in SPLV). Values closer to zero indicate reduced electrostatic repulsion, suggesting a higher likelihood of aggregation, but also highlight the role of the coating in modulating surface charge and stability.[12,32,50] Overall, DLS and ζ-potential data show that hydrodynamic behaviour and colloidal stability are strongly influenced by the coating type, Au content, and Gd functionalization. Plant-extract-based SPIONs display higher heterogeneity but greater functionalization potential compared to dextran-coated analogues. For completeness, the histograms representing size distributions by number and by intensity, as well as the zeta potential profiles, are presented in the SI (Fig. S5 and S6).

^{57}Fe Mössbauer spectroscopy

As in the case of the SP_{pH} samples reported in Ferreira-Filho *et al.*[12] ^{57}Fe Mössbauer spectroscopy measurements of the present SP-LV-Au1 and SP-LV-Au1–Gd samples were carried out in order to better characterize the SPIONs, based on the iron coordination and oxidation state. Concerning SP-LV-Au3 and SP-LV-Au3–Gd samples, in spite of very long accumulation times, the spectra (not shown) had a very low signal to noise ratio, too low to allow an accurate analysis of the fraction of Fe in magnetite and maghemite domains. This may be explained by the low Fe content compared to that of gold in these samples. Since gold is the element with the highest mass absorption coefficient for the 14.4 keV radiation, it strongly reduces the 14.4 keV beam intensity.

The spectra of the SP-LV-Au1 and SP-LV-Au1–Gd samples (Fig. 3) are similar to those of SPpH-Dx-Au and SPpH-Dx-Au–Gd taken at room temperature revealing similar magnetic relaxation frequencies. They were therefore fitted by three magnetic splittings. As previously explained in detail,[12] one of the sextets is typical of the fast electron hopping observed between Fe^{2+} and Fe^{3+} on the octahedral sites of magnetite above the Verwey transition (Table 2). These Fe cations are usually reported as $Fe^{2.5+}$.[51–53] The remaining two sextets are consistent with Fe^{3+} on octahedral sites of maghemite and unresolved contributions of Fe^{3+} on tetrahedral sites of both magnetite and maghemite domains. Mössbauer data suggest, therefore, that in both SP-LV samples, similar amounts, approximately 42–44%, of the Fe cations are located in magnetite domains while the remaining Fe cations are on maghemite domains.

Table 1 SPIONs' crystallite size obtained from PXRD; particle size and dispersion from TEM; magnetic diameter from SQUID; hydrodynamic size and zeta potential (ζ) from DLS measurements

Sample	Crystallite size (nm) – PXRD	Particle size – DTEM (nm)	Magnetic diameter (nm) – SQUID	Size dispersion – σ (%)	Hydrodynamic size – DH (nm) (PDI)	ζ (mV)
SPpH[12]	10.0 ± 0.5	12.2 ± 2.5	10.09	20.84	25.4 (0.5)	43.8 ± 10
SP-Dx[12]	12.0 ± 0.6	16.5 ± 4.1	9.46	24.80	136.1 (0.6)	−15.1 ± 1.3
SP-Dx-Au[12]	18.2 ± 0.9	19.4 ± 5.6	9.65	28.62	28.2 (0.7)	−21.5 ± 0.7
SP-Dx-Au–Gd[12]	18.3 ± 1.3	20.0 ± 5.0	10.9	25.18	42.5 (0.5)	−16.7 ± 0.7
SP-LV-Au3	18.7 ± 1.2	18.4 ± 4.6	14.5	24.74	40.8 (0.5)	−25.3 ± 0.2
SP-LV-Au3–Gd	18.7 ± 1.3	21.1 ± 5.7	14.5	26.91	45.3 (0.6)	−6.9 ± 0.7
SP-LV-Au1	18.4 ± 1.8	14.5 ± 4.6	12	30.93	33.2 (0.6)	−36.5 ± 0.2
SP-LV-Au1–Gd	18.4 ± 1.8	26.2 ± 7.0	13.8	26.18	29.2 (0.5)	−3.2 ± 0.1

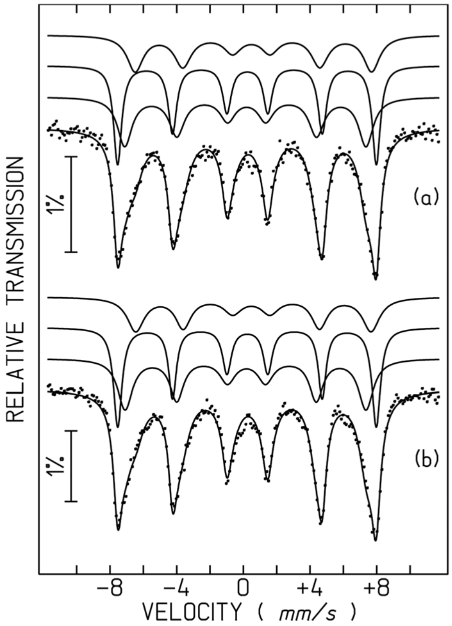

Fig. 3 Mössbauer spectra of (a) SP-LV-Au1 and (b) SP-LV-Au1–Gd taken at room temperature. Calculated lines on the experimental points are the sum of three sextets (Table 2).

SQUID magnetometry

The magnetic properties of the SPION samples obtained by the green approach were measured and parameters such as saturation of magnetization ($M_{\mathrm{Sat.}}$) and blocking temperature (T_B) were determined. To better evaluate the potential magnetic behaviour of the samples, analyses of the temperature dependence of the magnetization at low fields and isothermal or field dependence of the magnetization were performed at a temperature closer to that of the human body, 300 K, and at a lower value, 10 K. The zero-field cooling and field cooling cycle (ZFC/FC) magnetization curves of SPION samples with leaf extracts are shown in Fig. 4.

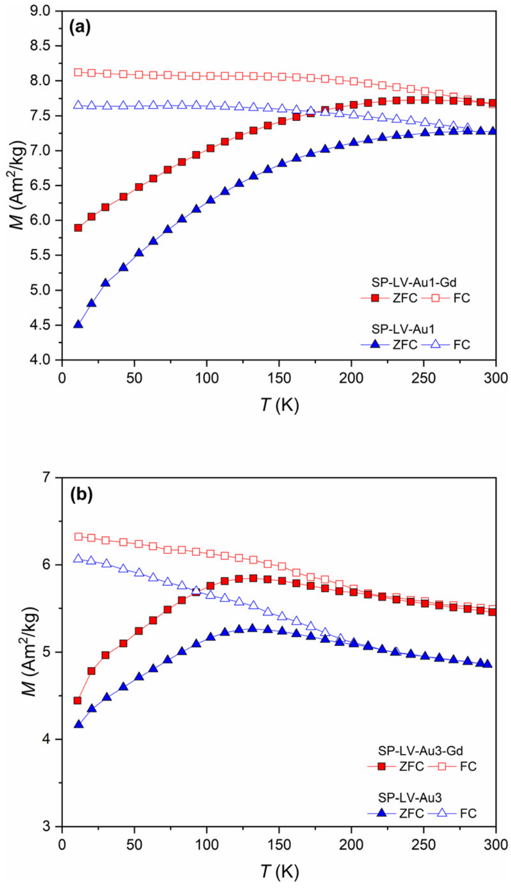

Fig. 4 Temperature dependence of the zero-field cooling (ZFC) and field cooling (FC) magnetization at 10 mT for (a) SP-LV-Au1–Gd, SP-LV-Au1, and (b) SP-LV-Au3–Gd and SP-LV-Au3.

Under the zero-field cooling conditions, the magnetization curves show a maximum more visible for some of the samples than others, resulting in a distribution of blocking temperatures, T_B, which depends on a less or more broad distribution of particle sizes, respectively. For the naked sample, SP, T_B was found to be approx. 150 K, which agrees with values found in the literature ranging from 126 K to 195 K.[11] When samples are cooled in the presence of a magnetic field (Field-Cooled (FC) plots, dotted lines) it can be seen that the magnetic signal

Table 2 Estimated parameters from the Mössbauer spectra of the SPION samples taken at room temperature

	IS (mm s^{-1})	ε (mm s^{-1})	B_{hf} (tesla)	I	Fe state	Fe in Fe_3O_4
SP[12]	0.26	−0.09	44.3	32%	Fe^{3+} CN = 4 γFe_2O_3, Fe_3O_4	33%
	0.33	0.01	48.6	47%	Fe^{3+} CN = 6 γFe_2O_3	
	0.66	0.26	42.8	21%	$Fe^{2.5+}$ CN = 6 Fe_3O_4	
SP-LV-Au1	0.27	−0.08	44.9	34%	Fe^{3+} CN = 4 γFe_2O_3, Fe_3O_4	44%
	0.34	−0.02	48.1	37%	Fe^{3+} CN = 6 γFe_2O_3	
	0.65	0.13	44.0	29%	$Fe^{2.5+}$ CN = 6 Fe_3O_4	
SP-LV-Au1–Gd	0.27	−0.06	44.8	35%	Fe^{3+} CN = 4 γFe_2O_3, Fe_3O_4	42%
	0.34	−0.02	48.1	37%	Fe^{3+} CN = 6 γFe_2O_3	
	0.65	0.12	43.8	28%	$Fe^{2.5+}$ CN = 6 Fe_3O_4	

IS: isomer shift relative to metallic α-Fe at 298 K; $\varepsilon = (e2QVzz/4)\,(3\cos 2\theta - 1)$ quadrupole shift; B_{hf}: magnetic hyperfine field; I relative area; CN: coordination number; estimated errors ≤ 0.02 mm s^{-1} for IS, ε, Γ, <0.3 T for B_{hf} and <2% for I.

is higher than the ZFC (Zero-Field-Cooled) values due to the freezing of the magnetic moments, which remain aligned along the field direction below the blocking temperature. Once T_B is exceeded, there is a further drop to match the ZFC plot. The irreversibility of ZFC and FC curves below T_B and the observation of broad maxima of the ZFC curves are characteristic of nanoparticles in a superparamagnetic state. The superparamagnetic state, characteristic of particles with very small dimensions, is here demonstrated by the irreversibility of the ZFC and FC curves, along with the broad maximum observed in the ZFC curve, despite some particle size distribution. In the case of larger nanoparticles, a higher temperature is required for the thermal energy to overcome the energy barrier, allowing them to exhibit superparamagnetic behaviour.[54–56] Estimated blocking temperatures T_B for all samples are shown in Table 3.

Fig. 5 shows the hysteresis loops obtained for these temperatures, 300 K (top) and 10 K (bottom). At room temperature, the absence of irreversibility in the hysteresis plot, along with the lack of magnetic remanence (MR), confirms the superparamagnetic behaviour of the nanoparticles. This is expected, as thermal energy at room temperature is sufficient to randomize the nanoparticle spins, preventing them from retaining magnetization once the external magnetic field is removed. However, at lower temperatures, such as 10 K, the situation changes. Below the blocking temperature, thermal energy becomes insufficient to randomize the spins as the field decreases, leading to a behaviour that deviates from superparamagnetism and the nanoparticles behave as ferrimagnetic, showing a small coercive field, HC, of −0.014, −0.015, −0.016 and −0.017 T for SP-LV-Au3, SP-LV-Au3–Gd, SP-LV-Au1, and SP-LV-Au1–Gd, respectively. This occurs when the energy barrier that prevents spin reorientation is no longer overcome by thermal fluctuations. Consequently, the particles can remain magnetized without an external field.[55–57] The blocking temperature marks the threshold at which thermal energy is sufficient to allow spin randomization; beyond this point superparamagnetism no longer persists. It should also be noted that the increase in magnetization in samples containing Gd exceeds that of the other samples (SP-LV-Au3 at 1 T and SP-LV-Au1 at 1.5 T) without reaching saturation at 5 T. This behaviour may be due to the presence of Gd, which exhibits a strong paramagnetic behaviour and contributes to the resulting magnetism.

Table 3 Magnetic properties of the SPION samples under study, at 10 K and 300 K

	$M_{Sat.}$ (A m^2 kg^{-1})			
Sample	10 K	300 K	% loss in $M_{Sat.}$ at 300 K	T_B (K)
SP[12]	74.90	64.20	—	91
SP-Dx[12]	73.68	63.90	0.47	82
SP-Dx-Au[12]	64.47	55.26	13.93	132
SP-Dx-Au–Gd[12]	64.02	49.16	23.43	140
SP-LV-Au3	27.51	23.47	63.44	132
SP-LV-Au3–Gd	33.52	22.13	65.53	132
SP-LV-Au1	47.12	39.10	39.10	280
SP-LV-Au1–Gd	61.40	31.49	50.95	—

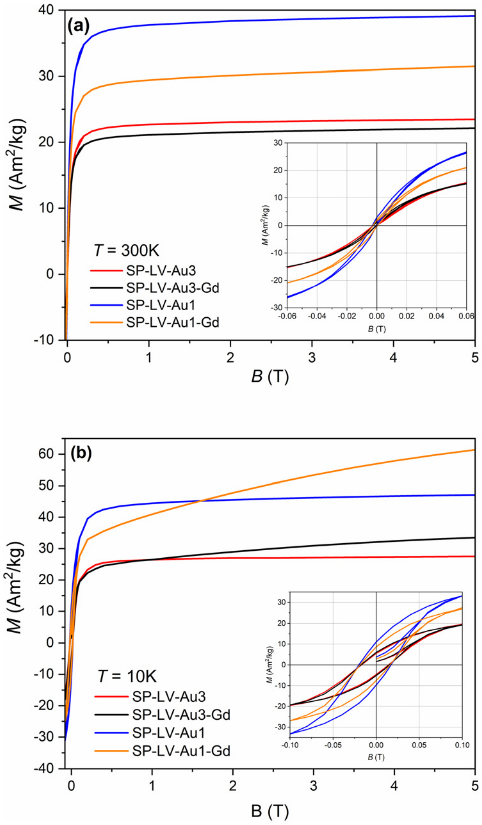

Fig. 5 Magnetic field (B) dependence of magnetization (M) for samples, SP-LV-Au1, SP-LV-Au1–Gd, SP-LV-Au3, and SP-LV-Au3–Gd, at (a) 300 K and (b) 10 K.

At 300 K the $M_{Sat.}$ value obtained for the naked SPION sample, taken as a reference, was 64.2 A m^2 kg^{-1}. As the SPION nanoplatform became more densely coated, the $M_{Sat.}$ decreased proportionally since coating may hinder the nanoparticles' magnetic ability to reach their maximum. As seen in Fig. 5 and Table 3, the 1 : 3 ratio leaf extract SPIONs (SP-LV-Au3 and SP-LV-Au3–Gd) have a lower M_{Sat} value consistent with the higher gold-to-iron ratio. There is a clear increase in M_{Sat} in the 1 : 1 ratio SPIONs (SP-LV-Au1 and SP-LV-Au1–Gd), which can be safely attributed to their lower gold content. The same tendencies of decreasing M_{Sat} as the SPION core gradually becomes more covered have already been observed for the dextran-coated route.[12] However, the saturation magnetization value of the sample SP-LV-Au1–Gd at 300 K, with M_{Sat} = 31.49 A m^2 kg^{-1}, is still slightly below the range used for MH. According to literature reports, effective MH requires M_{Sat} values ranging from 40 to 70 A m^2 kg^{-1}.[11,58–62] Nevertheless, these results do not invalidate the research on the green route synthesis of Au and Gd coated SPIONs, since the value obtained was only about 20% lower and the confirmation of the superparamagnetic behaviour is still promising, as confirmed below from the magnetic hyperthermia results.

Concerning the magnetization losses at room temperature, the estimated values are comparable or even lower than the values found in the literature, where coated SPIONs were found to lose between 40 and 44% of their $M_{\text{Sat.}}$ value after Au coating.[42,43]

With the information given by the magnetic parameters, $M_{\text{Sat.}}$ and T_B, based on the $M(B)$ curves obtained at 300 K it is possible to calculate the magnetic diameter of the samples (D_{mag}). This is done using the Langevin model according to eqn (1), where K_B is the Boltzmann constant (1.381×10^{-23} m^2 kg s^{-2} K^{-1}), ρ is the density of the iron oxide structure (4900 kg m^{-3} for simplification considering that the crystal structure is 100% maghemite) and $\left(\frac{\mathrm{d}M}{\mathrm{d}B}\right)_{B\to 0}$ is the derivative of the $M(B)$ curve when the magnetic field (B) tends to zero.

$$D_{\text{mag}} = \left(\frac{18K_B T\left(\frac{\mathrm{d}M}{\mathrm{d}B}\right)_{(B\to 0)}}{\pi\rho M_{\text{Sat.}}{}^2}\right)^{\frac{1}{3}} \quad (1)$$

These results are presented in Table 2 and compared to the ones already determined by the DLS, TEM and PXRD analyses.

Typically, magnetic diameters are found to be slightly smaller than the physical diameters of nanoparticles. This is explained by the presence of a "magnetically dead layer" on the NPs' surface, composed of disordered spins and with a zero-net magnetization.[63–65] According to the values in Table 1, naked SPIONs (SP) have the most discrete layer of magnetically disordered dipoles among the samples. This value gradually increases as the NPs are further coated, which affects the magnetic properties of the samples.

Relaxometric studies

The magnetic resonance (MR) contrast capability of both naked (SP) and hybrid SPIONs was assessed to determine their potential as image enhancement tools. Table 4 shows the relaxivity values obtained, by calculating the T_1 and T_2 values from T_1 and T_2 maps generated from the images obtained at 7 T (room temperature, Fig. 6); using the Gd concentration for the r_1 determination and the Fe concentration for r_2. Gd and Fe concentrations were assessed by ICP-OES. A sample of water has also been measured to determine the diamagnetic contribution of the solvent and this value was used for the relaxivity determination. To understand the influence of both metals in these parameters, the relaxivities and the ratio r_2/r_1 were also calculated using the total metal concentration "Gd + Fe".

Table 4 Longitudinal (r_1) and transverse (r_2) relaxivity values determined for samples of NP at 7 T (300 MHz, room temperature) and r_2/r_1 ratios

	7 T (300 MHz, room temp.)/mM^{-1} s^{-1}			
Sample	r_1	r_2	r_2/r_1	r_2/r_1 (Gd + Fe)
SP[12]	—	186	—	240
SP-DX-Au–Gd[12]	55	56	1.0	282
SP-LV-Au1–Gd	9.2	10.0	1.1	8
SP-LV-Au3–Gd	6.5	6.2	0.95	19

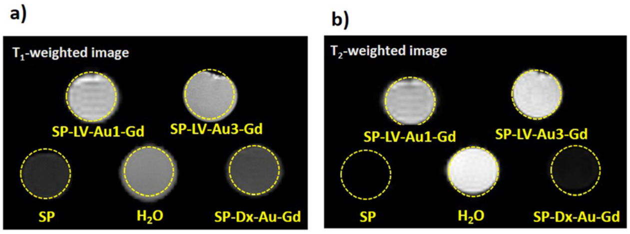

Fig. 6 7 T MR images of phantom tubes of samples SP, SP-Dx-Au–Gd, and SP-LV-Au1–Gd and SP-LV-Au3–Gd, as well as a water sample for comparison: (a) T_1-weighted images acquired at TE/TR = 21/626 ms and (b) T_2-weighted images acquired at TE/TR = 80/2000 ms.

Gadolinium-based probes serve as T_1 contrast agents, also known as positive contrast agents. They operate by shortening longitudinal relaxation times, resulting in bright signals in the acquired images. On the other hand, the SPIONs' iron oxide core provides a negative contrast, T_2, by shortening proton transverse relaxation times, which appears as dark signals in the images.[66] The parameter of longitudinal/transverse relaxivity (r_1 or r_2) indicates the potential for signal enhancement, in the presence of 1 mM Gd^{3+} or Fe$^{2+/3+}$, respectively. Additionally, the ratio r_2/r_1 serves as an indicator of a contrast agent's suitability for either positive (T_1) or negative (T_2) contrast applications, or both. With this knowledge, it is possible to see the contribution of Gd in its r_1 in Table 4.

The particles studied display a longitudinal relaxivity with values higher than those of contrasts in clinical use (3.4 to 4.6 mM^{-1} s^{-1} at 1 T (42 MHz), 37 °C). Concerning transverse relaxivities (r_2), although the magnetic field plays an important role, the values determined are considerably lower than the ones reported for negative contrast probes Sinerem, Feridex or Resovist: 88, 120 and 186 mM^{-1} s^{-1}, respectively, at 1.5 T.[67] The only exception is naked SPIONs, whose relaxivity is 186 mM^{-1} s^{-1} at 7 T. Upon coating, the r_2 values drop, but are still comparable with those of other gold nanoparticles functionalized with gadolinium found in the literature, measured at the same magnetic field (7 T): 4.7 mM^{-1} s^{-1} for Lip-DO3A@AuNP[68] or Gd–Au-SPIONs which have an r_1 of 43.6 mM^{-1} s^{-1} and an r_2 of 123 mM^{-1} s^{-1}.[69] Relaxivities of other Au-containing nanoparticles have been studied at different magnetic fields: r_2 = 29–38 mM^{-1} s^{-1} at 0.47 T (20 MHz) and r_1 = 10–12 mM^{-1} s^{-1} at 4.7 T (200 MHz) for DO3A-aminopropionate-based AuNPs,[70] and an r_1 of 14.6 mM^{-1} s^{-1} and an r_2 of 38.5 mM^{-1} s^{-1} DNA-Gd@AuNP (measured at 1.4 T and 37 °C).[71]

Table 4 also depicts the r_2/r_1 ratio. The transverse-to-longitudinal relaxivity ratio (r_2/r_1) smaller than 2 for samples SP-DX-Au–Gd, SP-LV-Au3–Gd and SP-LV-Au1–Gd means that they can also be considered as positive, T_1-contrast agents.[72] Nevertheless, herein the presence of high iron content highly impacts the overall relaxivity and the T_1-effect is nearly suppressed in view of the strong T_2-effect. This is visible when looking into the phantom images obtained (Fig. 6), as well as considering the r_2/r_1 ratio calculated using the total amount of metal "Gd + Fe", which has also been observed by other authors.[69] The particles can then act as a T_2-based contrast agent, with once again evidence of the influence of the coating lowering the relaxivities.

Magnetic hyperthermia

All SPION-based samples were subjected to an alternating magnetic field (AMF) with an amplitude of 16 kA m^{-1} and a frequency of 140 kHz (Fig. 7). These parameters were selected based on extensive optimization, as previously reported.[12] The thermal response of the nanoparticles was recorded, including an initial temperature stabilization period of 1 minute, followed by heating until thermal saturation. Representative heating curves for the samples are shown in Fig. 7, and were fitted using the Box–Lucas model to extract the Specific Absorption Rate (SAR) values.[12,73] The resulting SAR values are summarized in Table 5. The highest SAR values were observed for the samples prepared by the classical method and coated with dextran (SP-Dx-Au and SP-Dx-Au–Gd). These samples exhibited SAR values of 57082 W g^{-1} and 97 673 W g^{-1}, respectively. The superior performance of these samples is attributed to their high magnetic moments ($M_{\text{Sat.}}$) and controlled particle size. Both SP-Dx-Au and SP-Dx-Au–Gd samples exhibited the highest saturation magnetization of 55.3 A m^2 kg^{-1} and 49.2 A m^2 kg^{-1}, respectively, combined with a small size that promotes efficient Néel/Brownian magnetic relaxation under AMF exposure.[74] In the Gd sample (SP-Dx-Au–Gd), the magnetic effect increases with the presence of Gd, even at low concentrations, despite the slight reduction in Fe content. This phenomenon is explained by the strong magnetic moment of Gd, a lanthanide with seven unpaired electrons, as well as by different surface effects that enhance the alignment of the magnetic moments and lead to the nanoparticle's overall magnetic response to an AMF by adding to the magnetic moment of the iron oxide core.[12,75] Additionally, the dextran coating contributes to improved colloidal stability and controlled interparticle spacing, further reducing magnetic dipolar interactions and energy conversion efficiency under AMF.[76]

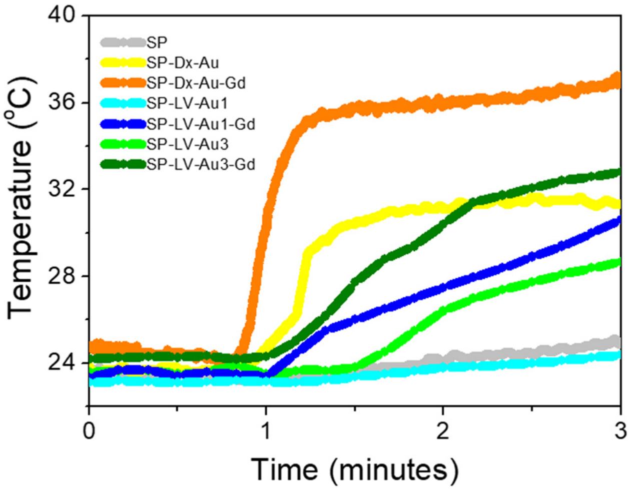

Fig. 7 Heating performance of SPION samples measured at f = 140 kHz and B = 16 kA m^{-1}.

Table 5 Specific absorption rate, SAR, values of samples at 16 kA m^{-1} and frequency of 140 kHz compared with the previously determined size and saturation magnetization

Sample	ΔT	SAR (W g^{-1})	DLS (nm)	M_{Sat} (A m^2 kg^{-1})
SP	1.6	934	25.4	64.2
SP-Dx-Au	7.6	57 082	28.2	55.3
SP-Dx-Au–Gd	12.4	97 673	42.5	49.2
SP-LV-Au1	1.1	2410	33.2	39.1
SP-LV-Au1–Gd	7.3	8015	29.2	31.5
SP-LV-Au3	5	391	48.2	23.5
SP-LV-Au3–Gd	8.6	4805	45.3	22.1

Notably, the green-synthesized samples (SP-LV-Au1–Gd and SP-LV-Au3–Gd), although characterized by lower $M_{\text{Sat.}}$ values, also showed significant SAR enhancement upon Gd incorporation. For instance, SAR increased from 2410 W g^{-1} (SP-LV-Au1) to 8015 W g^{-1} in the Gd-modified version, and from 391 W g^{-1} (SP-LV-Au3) to 4805 W g^{-1} in its Gd-containing counterpart. This indicates that the presence of Gd plays also a pivotal role in improving magnetic heating efficiency in the green-synthesized samples as discussed for the SP-Dx-Au–Gd sample. Furthermore, the incorporation of Gd leads to an increase in nanoparticle size, as observed in TEM data (*e.g.*, from 14.5 nm to 26.2 nm in SP-LV-Au1 *vs.* SP-LV-Au1–Gd), which can positively affect Néel and Brownian relaxation mechanisms, particularly in the superparamagnetic size regime. This effect is particularly evident in SP-LV-Au1–Gd, where a relatively high Gd concentration (23%) results in a significantly enlarged nanoparticle core (26.2 nm TEM size) and enhanced SAR. Despite the reduced $M_{\text{Sat.}}$, the increased volume and altered surface magnetism allow the particles to absorb and dissipate energy more efficiently under AMF exposure.

Cell studies

Cell studies with ^{60}Co γ-rays

Cell irradiation studies with ^{60}Co γ-rays in the presence of the SPION-nanoplatforms were performed in both human prostate cancer cells (PC3) and non-tumorigenic prostate epithelial cells (RWPE-1). Preliminary assays were carried out to determine the appropriate concentration(s) for the radiosensitisation studies. For all nanoplatforms, a concentration of 20 µg Fe mL^{-1} was selected, as it provided the best compromise between cellular tolerance and the absence of interference with the MTT colorimetric assay used to evaluate cell viability (Fig. S8).

For the non-irradiated RWPE-1, no appreciable loss of viability was observed after 24 h of incubation at 20 µg Fe per mL

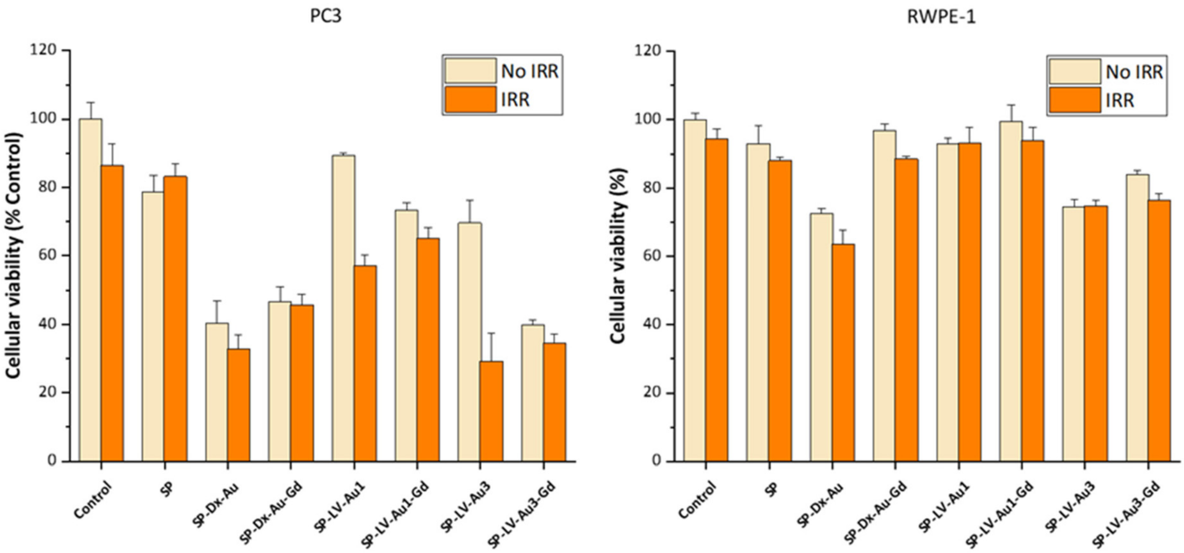

Fig. 8 Cellular viability of PC3 and RWPE-1 cells treated with the different nanoplatforms at 20 μg mL^{-1} and irradiated with γ-rays (2 Gy, total dose). Cellular viability was determined by the MTT assay, 72 h after irradiation. Results are expressed as mean ± SD (n = 4).

for any formulation, with the exception of SP-Dx-Au. In contrast, PC3 cells presented an appreciable decrease in viability at the same concentration for the dextran- and Gd-containing nanoplatforms, with the strongest effect observed for SP-Dx-Au, while a similar behaviour was also observed for SP-LV-Au3–Gd, which exhibited the more pronounced effect of all nanoplatforms (Fig. 8 and S8).

After exposure to ^{60}Co γ-radiation (1 Gy min^{-1}, 2 min, 2 Gy), the reduction in viability was clearly cell-type dependent (Fig. 8). Non-tumoral RWPE-1 cells showed little to no decrease across all formulations, whereas PC3 cells exhibited pronounced responses for certain nanoplatforms. Among the dextran-based platforms, the radiation effect was generally modest, with SP-Dx-Au showing the most notable decrease (Fig. 8). PC3 cells treated with SP-LV-Au1 and SP-LV-Au3 displayed marked radiosensitisation. SP-LV-Au1 showed a 32% reduction in viability compared with that under non-irradiated conditions (89.5 ± 0.7% *vs.* 57.2 ± 3.1%); while SP-LV-Au3 exhibited the stronger effect (69.7 ± 6.5% to 29.2 ± 8.3%; Fig. 8 and S9).

Interestingly, the reduction in viability was less pronounced for the Gd-containing nanoplatforms compared with their Au-only precursors (Fig. 8). This attenuation is partly due to the higher intrinsic cytotoxicity of the Gd-bearing formulations, which reduces the dynamic range for detecting additional radiation-induced cell death. Although both Au and Gd are high-Z elements capable of generating secondary radiation, the effectiveness of dose enhancement depends on both the atomic number and local concentration. The elemental composition, as determined by PIXE, offers additional insight: in SP-LV-A1 and SP-LV-Au1–Gd, Au contents are similar (9.2% *vs.* 8.2%), and despite the substantial Gd content in SP-LV-Au1–Gd (22.8%), radiosensitisation is not increased, indicating that under Compton-dominated ^{60}Co γ-radiation, Au remains the main contributor to secondary electron production. In SP-LV-A3 and SP-LV-Au3–Gd, the Au-only platform contains significantly more Au (39.8% *vs.* 26.3%), while the Gd content in SP-LV-Au3–Gd is low (4.1%).

The strong radiosensitisation observed in SP-LV-Au3 further confirms that Au concentration largely dictates dose enhancement under these conditions. Taken together, these results suggest that the radiosensitising effect under ^{60}Co γ-ray irradiation is primarily driven by Au content, with little contribution of Gd. Additional factors, such as subcellular localisation and intracellular distribution, may further modulate the effectiveness of secondary electron-mediated damage, particularly in platforms where Au is partially replaced or diluted by Gd.

ROS production by ^{60}Co γ-radiation

Nanoparticles, particularly those based on gold, are well known as radioenhancers that can improve the efficacy of cancer treatments using both non-ionizing and ionizing (radiotherapy) energy-based therapies.[77] One of the key effects induced by radiotherapy is the production of reactive oxygen species (ROS), which contribute to cellular damage. As shown in Fig. 9, cells treated with SP-LV-Au1 and SP-LV-Au3 exhibit increased ROS production in a concentration-dependent manner, which is further enhanced upon γ-irradiation. The presence of iron in the SPIONs likely contributes to this effect, particularly in SP-LV-Au3 at 3 h post-irradiation, probably *via* iron-catalyzed Fenton and Haber–Weiss reactions between hydrogen peroxide (H_2O_2) and Fe^{2+}, leading to the formation of hydroxide (OH^-) and highly reactive hydroxyl radicals ($OH^\bullet$).[78]

Transmission electron microscopy – TEM studies

The analysis of morphological alterations in PC3 cells was performed by TEM using untreated cells and cells treated with SP-LV-Au3, with and without γ-irradiation (^{60}Co γ-rays, 2 Gy)

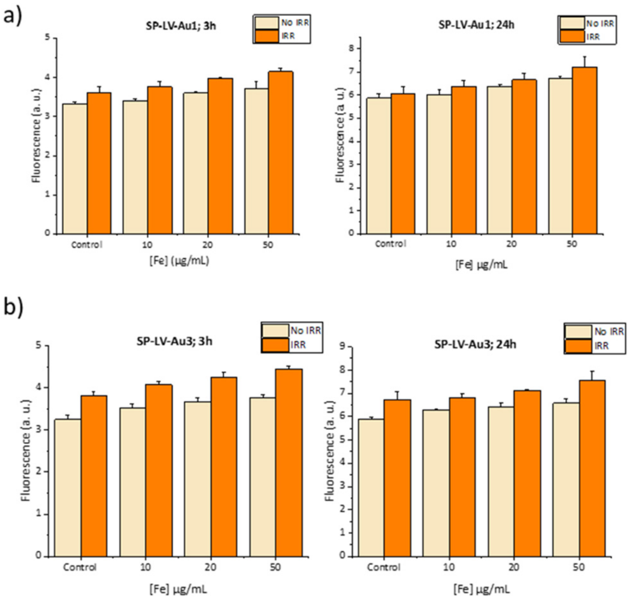

Fig. 9 Fluorescence signal of DCF in PC3 cells under control and ^{60}Co γ-radiation conditions. After incubation with SP-LV-Au1 (a) or SP-LV-Au3 (b), at 10, 20 and 50 µg Fe per mL and γ-irradiation (2 Gy). The fluorescence measurements are performed at 3 h and 24 h post-irradiation. Controls represent cells with/without irradiation only. Results (in arbitrary units) are the mean ± SD of three independent experiments.

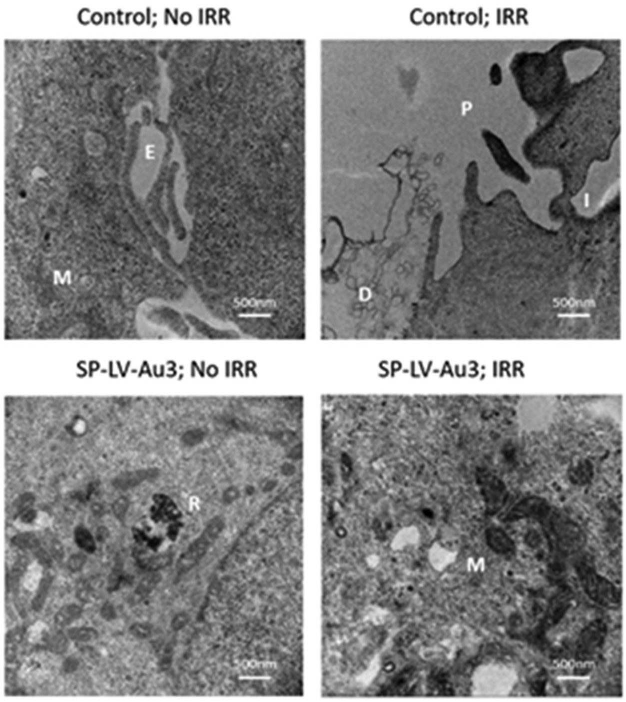

Fig. 10 Transmission electron microscopy (TEM) analysis of morphological alterations in PC3 cells before and 2 h after irradiation with ^{60}Co γ-rays. The panel includes untreated control cells (non-irradiated and irradiated) and cells treated with SP-LV-Au3 for 24 h (non-irradiated and irradiated). Samples were analyzed and imaged using a FEI Tecnai G2 Spirit BioTWIN transmission electron microscope. E = extracellular space; M = mitochondria; P = membrane projections; I = membrane invaginations; D = dying cell; and R = vacuoles containing cellular debris. Scale bar: 500 nm.

(Fig. 10). SP-LV-Au3 was selected for these studies based on its pronounced radiosensitising effect in PC3 cells, which was stronger than that observed for the other nanoplatforms (see above). Owing to its robust and dose-dependent response to γ-irradiation, SP-LV-Au3 was considered the most suitable platform for examining radiation-induced ultrastructural damage and nanoparticle–cell interactions at the subcellular level.

The results show that under control conditions, untreated PC3 cells display normal morphology. In contrast, irradiated untreated cells exhibit an irregular cell surface, prominent membrane projections, and membrane invagination. Cells treated with SP-LV-Au3 without γ-irradiation present numerous vacuoles containing cellular debris, including damaged organelles and cytoplasmic material. This suggests activation of autophagic processes, a cellular mechanism involved in the degradation and recycling of compromised intracellular components. In γ-irradiated SP-LV-Au3-treated cells, pronounced mitochondrial alterations were observed, including dense matrix appearance and a disrupted morphology, which are indicative of oxidative stress and impaired cellular homeostasis, consistent with the increased ROS production described above.

Cell studies with magnetic hyperthermia

Magnetic hyperthermia (MH)-induced cytotoxicity was evaluated in human prostate cancer (PC3) and normal prostate epithelial (RWPE-1) cells using all nanoplatforms. Experiments were performed at an optimized nanoparticle concentration of 20 µg Fe per mL under an alternating magnetic field (AMF) of 16 kA m^{-1} and a frequency of 140 kHz for 30 minutes. Under no-MH conditions, both the SP precursor and the green SP-LV nanoplatforms lacking Gd maintained high viability in PC3 cells, confirming negligible intrinsic toxicity; this outcome is consistent with the trends observed during ^{60}Co γ-ray irradiation. In contrast, the dextran-based nanoplatforms (SP-Dx-Au and SP-Dx-Au–Gd) as well as the Gd-containing SP-LV formulations—particularly SP-LV-Au3–Gd—exhibited some intrinsic cytotoxicity. No appreciable toxicity was detected in non-tumoral RWPE-1 cells (Fig. 11a), underscoring their selective effects toward cancer cells.

Upon MH exposure, Gd-containing nanoplatforms consistently exhibited enhanced cytotoxic effects in PC3 cells, in line with the trends observed in the SAR measurements (see the discussion on magnetic hyperthermia above). The most pronounced MH-induced cytotoxicity was observed for SP-Dx-Au–Gd, SP-LV-Au1–Gd, and SP-LV-Au3–Gd. In particular, SP-LV-Au3–Gd caused a sharp decrease in cell viability at 24 h, becoming even more pronounced after 48 h, demonstrating the strong MH-mediated cytotoxic potential of this nanoplatform. This highlights the relevance of the effect after the exposure and indicates that Gd incorporation significantly amplifies cytotoxicity due to the Néel and Brownian relaxation that facilitates energy dissipation under AMF exposure

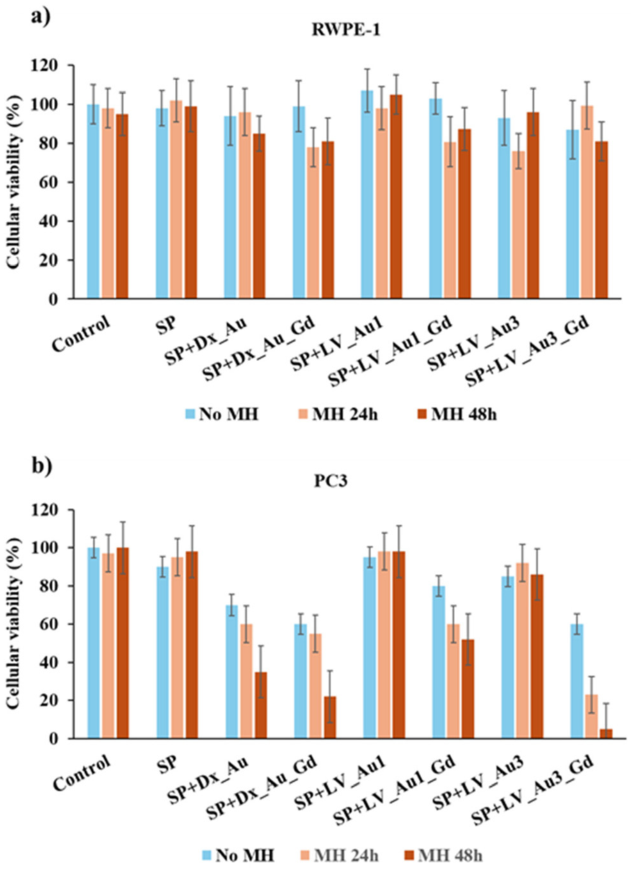

Fig. 11 Cellular viability of RWPE-1 (a) and PC3 (b) prostate cell lines treated with the different nanoplatforms at 20 μg mL^{-1} and subjected to an alternating magnetic field (AMF) of 16 kA m^{-1} and a frequency of 140 kHz for 30 minutes.

(Fig. 11b). TEM data further show that the presence of Gd enlarges the nanoparticle cores (*e.g.*, from 14.5 nm to 26.2 nm in SP-LV-Au1 *vs.* SP-LV-Au1–Gd), which enhances heating efficiency. The SAR values reflect these effects: SP-Dx-Au–Gd exhibits the highest SAR (97 673 W kg^{-1}), while SP-LV-Au1–Gd (8015 W kg^{-1}) and SP-LV-Au3–Gd (4805 W kg^{-1}) show significantly higher values than their Au-only counterparts (2410 W kg^{-1} for SP-LV-Au1 and 391 W kg^{-1} for SP-LV-Au3). These findings confirm the effectiveness of these nanoplatforms in inducing cancer cell death through MH and highlight the importance of the exposure duration for achieving therapeutic outcomes. This behaviour is markedly different from that of ^{60}Co γ-irradiation, where Gd contributes minimally and radiosensitisation is primarily dictated by Au content.

In contrast, the RWPE-1 normal prostate cells exhibited a markedly different response to the same treatments (Fig. 11). Across all conditions—including 24 and 48 hours of MH exposure—cell viability remained high (>80%), with no statistically significant reductions observed for any of the nanoplatforms. This demonstrates that the MH-induced cytotoxic effects observed in PC3 cells are selective and do not extend to non-cancerous cells under the same conditions.

Overall, these findings indicate that certain nanoplatforms, particularly SP-LV-Au3–Gd, are effective in selectively inducing death in cancer cells *via* MH while sparing normal cells, a desirable characteristic for potential therapeutic applications. The selective cytotoxicity, enhanced over time, suggests that these systems could be further optimized for clinical hyperthermia treatments in prostate cancer.

ROS production by magnetic hyperthermia

To investigate whether oxidative stress contributed to the magnetic-hyperthermia-induced cytotoxicity observed in PC3 cells, intracellular ROS levels were quantified 3 h and 24 h after incubation with FITC-labelled nanoparticles (corresponding to 24 h and 48 h after MH exposure, respectively). This analysis was particularly relevant given that several mechanisms associated with MH—local temperature, membrane perturbation, metal-mediated redox reactions, and mitochondrial stress—may trigger secondary ROS generation, potentially contributing to cell death pathways.[79] However, the ROS data (Fig. 12) do not indicate any pronounced or systematic increase in oxidative stress across the nanoplatforms following MH treatment. This observation is consistent with previous reports indicating that, although magnetic hyperthermia may induce cell death through multiple pathways, the contribution of oxidative stress is highly dependent on experimental conditions and is not always the dominant mechanism.[80,81] Moreover, MNPs have been reported to exhibit dual redox behavior, acting either as ROS promoters or scavengers, and the precise molecular mechanisms underlying these effects remain not fully elucidated.[81] The clearest ROS elevation is observed for the uncoated SP sample, particularly at 24 h, whereas this effect is largely attenuated once the particles are dextran-coated (SP-Dx-Au and SP-Dx-Au–Gd). Modest ROS increases are also detected in some leaf-extract-derived platforms—most noticeably SP-LV-Au1–Gd and SP-LV-Au3—but these changes remain small and are not consistent across all time points. Importantly, the Gd-containing nanoplatforms—which exhibi-

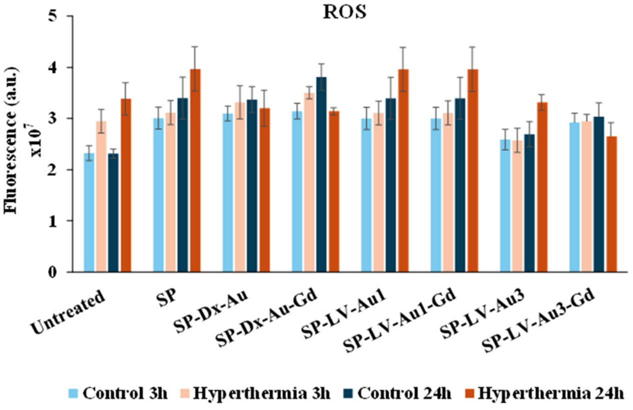

Fig. 12 Fluorescence signal of FITC in PC3 cells under control and hyperthermia conditions. Results (in arbitrary units) are expressed as mean ± SD (n = 4).

ted the strongest MH-induced cytotoxicity—do not display a corresponding rise in ROS levels. SP-LV-Au1–Gd induces minor ROS variations at 24 h, whereas SP-Dx-Au–Gd shows a slight increase at 3 h; SP-LV-Au3–Gd, in contrast, produces no appreciable ROS at any time point. Overall, although Gd incorporation does not generally enhance ROS production, certain formulations—such as SP-LV-Au1–Gd (24 h) and SP-Dx-Au–Gd (3 h)—still display subtle redox activity, which may reflect weak electron-transfer events or secondary oxidative reactions under specific nanoparticle configurations.[82]

Taken together, these observations indicate that ROS production is not a major contributor to the MH-induced cytotoxicity observed for the Gd-bearing nanoplatforms. Instead, the biological effects are more likely driven by efficient magnetic heating, consistent with the high SAR values of these systems, rather than by oxidative stress or redox-mediated pathways. Thus, while mild ROS elevation is detectable in a few formulations—possibly reflecting secondary metabolic stress following MH exposure—the overall pattern demonstrates that ROS generation does not correlate with the cytotoxicity trends, reinforcing the conclusion that Gd-enhanced magnetic relaxation and heating efficiency, rather than oxidative stress, are the primary determinants of PC3 cell susceptibility under AMF.

Conclusions

The green SPION–Au and SPION–Au–Gd hybrid nanoplatforms demonstrate complementary theranostic functionalities, with distinct mechanisms prevailing under ^{60}Co γ-irradiation *versus* magnetic hyperthermia (MH), alongside measurable MRI contrast capabilities. Radiosensitization is primarily Au-driven, resulting in ROS-dependent cytotoxicity and characteristic ultrastructural damage in PC3 prostate cancer cells, while sparing non-tumoral RWPE-1 cells. In contrast, under MH, Gd incorporation dominates cytotoxicity through enhanced SAR, increased magnetic disorder, and enlarged nanoparticle cores, inducing efficient, time-dependent, and ROS-independent cell death selectively in cancer cells. Relaxometric measurements further reveal that, although the presence of Gd increases r_1, the strong T_2 contribution from the iron oxide cores prevails. The hybrid platforms thus operate primarily as T_2-weighted MRI contrast agents, which could enable their use for imaging-guided therapy.

Future optimization of synthesis parameters and reagent proportions could increase saturation magnetization ($M_{\text{Sat.}}$), further enhancing MH efficiency while maintaining biocompatibility and nanoparticle targeting capabilities. It is expected that these adjustments would also influence the radiosensitizing potential of the nanoplatforms by modulating Au content and distribution, as well as their MRI contrast performance through changes in core size, magnetic properties, and surface coating. This correlation between magnetic, compositional, and structural features emphasizes the importance of balancing magnetization, surface chemistry, and nanoparticle architecture to achieve optimal, multifunctional, and biocompatible theranostic outcomes.

Overall, this dual behaviour—Au-driven radiosensitization and Gd-enhanced MH—combined with MRI visibility, positions the green SPION–Au and SPION–Au–Gd nanoplatforms as promising candidates for multimodal theranostic applications in prostate cancer treatment.

Experimental

Materials and methods

Materials. All chemicals and solvents were of reagent grade and were used without additional purification, unless stated otherwise. Milli-Q water was produced from a Millipore system Milli-Q ≥18 MΩ cm (with a Millipak membrane filter 0.22 μm). Iron(III) chloride hexahydrate ($FeCl_3·6H_2O$), iron(II) chloride tetrahydrate ($FeCl_2·4H_2O$), sodium sulfite ($NaSO_3$), ammonia solution (NH_3 25%), hydrochloric acid (HCl, 37%), sodium hydroxide in pellets (NaOH), tetrachloroauric(III) acid trihydrate 99% ($HAuCl_4·3H_2O$), sodium borohydride ($NaBH_4$), and gadolinium(III) chloride ($GdCl_3·6H_2O$) were purchased from Aldrich Chemical.

Leaves of the Danube Delta *Nymphaea alba* species were obtained from the Biosphere Reserve of Romania. The leaf extracts were prepared at the Faculty of Sciences and Environment, Department of Chemistry, Physics and Environment, "Dunărea de Jos" University of Galati.[29]

The naked SPIONs (SP) used as a starting material for the nanoplatforms were synthesized by the co-precipitation process at controlled pH (pH = 9.6).[12]

The ligand 2-[4,7-bis(carboxymethyl)-10-[2-(3-sulfanylpropanoylamino)ethyl]-1,4,7,10-tetrazacyclododec1yl]acetic acid (TDOTA) was synthesized as previously reported.[83,84] The PC3 and RWPE-1 cell lines were obtained from ATCC, Manassas, VA, USA.

Synthesis of the multifunctional green SPION nanoplatform

Preparation of leaf extract. 1 g powdered *Nymphaea alba* leaf extract was dispersed in 100 mL Milli-Q water and stirred for 1 h at 40 °C. The obtained dispersion was cooled down to room temperature, subjected to double filtration with Whatman no. 1 filter paper, and used immediately.

Synthesis of *Nymphaea alba* leaf–gold coated SPION SP-LV-Au

The coating of naked SPIONs (SP) with *Nymphaea alba* leaf extract (extract LV) and gold was adapted from the method of Norouz Dizaji *et al.*[84] The different SPION/leaf extract/gold ratios used are listed in Table 6. Briefly, a solution of $HAuCl_4$ was added to a suspension of SP dispersed in Milli-Q water, followed by the slow addition of *N. alba* leaf extract. The mixture gradually changed from an initial yellow-brown to a reddish color (pH 2–3). After 30 minutes, $NaBH_4$ was added to increase the pH to approximately 7, and the reaction mixture was stirred for 7 hours at room temperature under protection from light. The resulting product was washed three times with

Table 6 Experimental conditions for the synthesis of green SPION-based nanoplatforms and corresponding acronyms

Acronym	Sample description	Precursor (mg)	Ext. LV (mL)	$HAuCl_4$ (mg)	TDOTA (mg)	$GdCl_3$ (mg)
SP_{pH}	SPIONs obtained by co-precipitation at pH = 9.6 (ref. 12)	—	—	—	—	—
SP-LV-Au3	SP coated Ext. LV Ext. : Au 1 : 3	SP (110)	25	169	—	—
SP-LV-Au3–Gd	SP-LV-Au3 Gd-functionalized	SP-LV-Au3 (219)	—	—	76	58
SP-LV-Au1	SP coated Ext. LV Ext. : Au 1 : 1	SP (102)	15	47	—	—
SP-LV-Au1–Gd	SP-LV-Au1 Gd-functionalized	SP-LV-Au1 (90)	—	—	36	39

Milli-Q water, centrifuged (5000 rpm, 10 min), and finally lyophilized.

Gadolinium functionalization of SP–LV–Au–Gd

A solution of TDOTA·2TFA in H_2O/EtOH (8 : 2) was slowly added to a suspension of SP-LV-Au in the same solvent mixture and stirred moderately for 7 h. One equivalent of $GdCl_3$ (relative to TDOTA) was then added dropwise. As Gd^{3+} complexation progressed, the pH gradually dropped due to TDOTA ligand deprotonation. The pH was continuously monitored and adjusted with NaOH to maintain it between 5.5 and 6. After stabilization, the reaction was allowed to proceed for 18 h. The resulting dispersion was washed with Milli-Q water and centrifuged at 5000 rpm for 10 min, until no free Gd^{3+} was detected by colorimetric titration with xylenol orange.[85] The product was freeze-dried for 48 h. Table 6 summarizes the experimental conditions used for the synthesis of the SPIONs in the green-leaf nanoplatforms.

Physicochemical characterization

UV-vis spectrophotometry (UV-vis). The SPIONs were dispersed in Milli-Q water at concentrations of 10 µg mL^{-1}. The scans were performed at room temperature in a Varian Cary 50 UV/Vis spectrophotometer in a quartz cell (path length = 1 cm) in the range 200–800 nm.

Attenuated total reflectance Fourier-transform infrared spectroscopy (ATR-FTIR). Fourier transform infrared (FTIR) spectra were recorded using a Thermo Fisher Scientific Nicolet iS50 spectrometer equipped with an ATR diamond crystal accessory (Thermo Fisher Scientific, Madison, WI, USA). Samples were prepared by mixing potassium bromide (KBr) with a small amount of the respective SPION samples using an agate mortar. Spectra were acquired at room temperature with a resolution of 4 cm^{-1}, accumulating 128 scans over the range of 4000 to 400 cm^{-1}.

Determination of the Fe, Au and Gd contents in SPIONs by PIXE. The gold (Au) content of the obtained nanoparticles was quantified in freeze-dried samples using the Particle Induced X-ray Emission (PIXE) technique, performed at the 2.5 MV Van de Graaff accelerator of IST using a 2.0 MeV proton beam. The detailed methodology regarding the PIXE set-up, quantitative analysis, and sample preparation have been described previously.[33] Briefly, freeze-dried SPIONs were microwave digested with a nitric acid/hydrochloric acid mixture (1 : 3 molar ratio) and yttrium (1000 mg L^{-1}) added as an internal standard. For each sample, three aliquots of 10 µL of the digested material were analysed. Elemental concentrations were expressed in mg kg^{-1} of dry weight.

Powder X-Ray diffraction (PXRD). The diffraction patterns of the nanoplatforms were recorded using a Bruker D2 Phaser diffractometer with a Cu Kα X-ray source (wavelength: 1.5406 Å). Data were collected from 10° to 80° (2θ) with a step size of 0.01°, rotating slowly to keep the powder stable on a silica wafer. Measurements were performed at 30 kV and 10 mA using a copper anode.

The patterns were analyzed with DIFFRAC.EVA software. Crystallite size was calculated using the Scherrer equation (2):

$$D_{\mathrm{XRD}} = \frac{K\lambda}{\beta \cos \theta} \tag{2}$$

where D_{XRD} is the crystallite size (nm), λ = 0.154 nm is the X-ray wavelength, θ is the Bragg angle, β is the full width at half maximum (FWHM) of the peak in radians, and K is the shape factor. In this study, K = 0.9 K was used, which is typical of spherical particles.[86]

Transmission electron microscopy (TEM). Transmission electron microscopy (TEM) images of the SPIONs were obtained with a FEI Tecnai G2 Spirit BioTWIN microscope at 120 keV at the Instituto Gulbenkian de Ciência – Electron Microscopy Facility. TEM samples were prepared in a sonicated suspension of concentration 500 µg mL^{-1}, in which a carbon-coated copper 300-mesh grid was dipped and left to dry for 5 minutes. Images were obtained on a FEI Tecnai G2 Spirit BioTWIN transmission electron microscope. Each image was analyzed using ImageJ (version 1.35J) and Origin software to determine the average diameter, size distribution, standard deviation, and size dispersion (σ). The equation used to calculate size dispersion is presented in eqn (3):

$$\sigma = 100 \times \frac{\text{standard deviation}}{\text{average size}} \tag{3}$$

Dynamic light scattering (DLS) and zeta potential. Hydrodynamic diameters of the SPIONs were determined using a Malvern Zetasizer Nano ZS (model ZEN 3600, Malvern Instruments, UK) with a 633 nm He–Ne laser, operating at an 173° angle. Samples dispersed in water at concentrations of 10 µg mL^{-1} were placed in disposable folded capillary zeta cells, which allows for the collection of hydrodynamic size dispersion and zeta potential determination immediately after. Each sample had two sets of 20 runs, also providing the polydispersity index (PDI). All the information from the tests was collected using the Zetasizer Software.

^{57}Fe Mössbauer spectroscopy. Mössbauer spectra of the SPION samples were collected at room temperature in transmission mode using a conventional constant acceleration spectrometer and a 25-mCi ^{57}Co source in the Rh matrix. The velocity scale was calibrated using an α-Fe foil at room temperature. Isomer shift values, IS, are given relative to this standard. The spectra were fitted to Lorentzian lines using a nonlinear least-squares method.[12,58] Relative areas and line widths of peak pairs 1–6, 2–5 and 3–4 in a magnetic sextet were constrained to remain equal during the refinement procedure.

Superconducting quantum interference device (SQUID) magnetometry. Magnetic results obtained by DC measurements were taken using a 6.5 T SQUID (Superconducting Quantum Interference Device) magnetometer from Cryogenic Ltd London, UK. The saturation of magnetization ($M_{\text{Sat.}}$) and the superparamagnetic behavior at room temperature were determined by the isothermal curves taken at temperatures of 300 K and 10 K using external magnetic fields up to 5 T. The mean magnetic diameter of the nanoparticles defined as D_{mag} was determined considering the $M(B)$ curves obtained at 300 K.

Measurements of the temperature dependence of the magnetization within the range of 5–310 K in the presence of an external magnetic field of 50 Oe were also performed with the data collected at increasing temperatures, from 10 to 300 K, after zero-field cooling and field cooling (ZFC/FC) cycles.

MRI phantoms. Magnetic resonance (MR) images of phantom tubes containing NP samples (0.14 ± 0.04 mg mL^{-1}) were recorded on a 7 T Pharmascan 70/16 superconducting magnet (Bruker, Wissembourg, France) with a shielded gradient set (230 mT m^{-1} maximum gradient amplitude) and a transmit–receive quadrature coil with an inner diameter of 38 mm and Paravision 5.0 software (Bruker BioSpin, Wissembourg). Images were acquired using a rapid spin echo sequence (RARE sequence, factor 8) with TE = 10; 20; 30; 40 and 50 ms and TR = 5.5; 3.0; 1.5; 0.8; 0.4; and 0.2 s. The resolution was 156×156 μm^2 with a matrix of 128×128 and an F.O.V. of 4.0×4.0 cm. The slice thickness was 1.0 mm. T_1 and T_2 maps were generated with Paravision software, and T_1 and T_2 values were calculated from these maps. All measurements were performed at room temperature and a tube containing water was measured under the same conditions for visual comparison and as diamagnetic contribution at 7 T. The Fe, Gd and Au concentrations were assessed by ICP-OES.

Elemental analysis using inductively coupled plasma optical emission spectroscopy (ICP-OES). For Inductively Coupled Plasma Optical Emission Spectroscopy (ICP-OES), samples with a concentration of 0.14 ± 0.0 mg mL^{-1} were sonicated for 60 minutes at room temperature. Spectrometric (ICP-OES) measurements were performed in an Agilent 5800 VDV spectrometer. Fe, Gd and Au standard solutions (Sigma-Aldrich) were prepared in a 5% aqua regia matrix (HNO_3 + HCl in a molar ratio of 1 : 3). A 200 μL sample of each NP solution prepared was digested following the protocol: (1) evaporation to dryness, (2) re-dissolving in 1 mL of aqua regia and evaporating to dryness, and (3) addition of 100 μL of H_2O_2 + 100 μL of H_2O, evaporating to dryness and finally retaking in 5 mL of 5% aqua regia for ICP measurements. The quantitative determinations were performed using the most accurate band: 342.246 nm for Gd; 259.940 nm for Fe and 267.594 nm for Au. All the measurements were done in triplicate.

Magnetic hyperthermia

The heating efficiency of SPION dispersion in water ([Fe] = 4 mM mL^{-1}) was assessed using an alternating magnetic field (AMF) generated by AC GEN from Nanotech Solutions. The AMF had a frequency from 45 to 180 kHz and a magnetic field strength from 5 to 200 Oe, applied for a duration of 5 minutes (maximum H.f. = 2.9×10^9 A m^{-1} s^{-1}). These experimental results conform to the safety guidelines proposed by Hergt and Dutz, adhering to the criterion of H.f. = 5×10^9 A m^{-1} s^{-1} for potential clinical applications of AMF.[87,88] A sample volume of 500 μL was introduced into Eppendorf tubes and individually positioned within the magnetic coils. Temperature changes were continuously monitored and recorded every second using a thermal infrared camera, located on the top of the coil cavity. The specific absorption rate (SAR) was calculated using the Box-Lucas's method.[73,89]

Cell studies

The human normal prostate RWPE-1 cells (ATCC CRL-3607) were cultured in keratinocyte medium supplemented with 10% FBS, BPE (bovine pituitary extract) and EGF (epidermal growth factor). The human prostate carcinoma PC3 cells (ATCC CRL-2505) were cultured in RPMI-1640 medium supplemented with 10% FBS. The cells were maintained at 37 °C under a humidified atmosphere of 5% CO_2. The culture media and supplements were purchased from Gibco (Thermo Fisher Scientific, MA, USA).

For the assays, cells were placed in 96-well plates at a density of 2×10^4 cells per well. After 24 h, the cells were incubated with suspensions of SPIONs in the range of 1–50 μg mL^{-1} prepared in complete medium, *i.e.*, keratinocyte medium for RWPE-1 and RPMI for the PC3 cells. Cell viability was measured after 24 h using the MTT colorimetric assay.[32] Cell viability was presented as the percentage of untreated cells (control cells) considered as 100% viable. Data represent the mean ± SD of four independent experiments.

Radiosensitising studies using ^{60}Co γ-rays

PC3 and RWPE-1 cells were seeded in 96-well plates at a density of 3×10^4 cells per well. The next day, the cells were incubated with 20 μg mL^{-1} suspensions of SPIONs in keratinocyte or RPMI complete media for 24 h. Cells were then irradiated with γ-rays using a ^{60}Co irradiator (PRECISA22, Pantatron Ltd. and Graviner Mfg. Co. Ltd., UK) at a dose of 2 Gy (1 Gy min^{-1}, 2 min). After irradiation, the medium was removed and replaced with fresh medium. After 72 h, cell viability was measured by the MTT assay. Values were presented as a percentage of untreated cells and non-irradiated cells (control cells) considered as 100% viable. Data represent the mean SD of four independent experiments. For the statistical analysis, a comparison of values was performed with a non-parametric *t* test using the GraphPad Prism *vs.* 6.0. (GraphPad Software, Inc., La Jolla, California, USA); *p*-values <0.05 were used to define statistical significance.

Detection of ROS using H_2DCF-DA

Intracellular ROS were measured using the H_2DCF-DA (dihydro-2′7′dichlorofluorescein diacetate) probe.[90]

Inside the cell, the probe is de-esterified and, upon oxidation with ROS, it turns to fluorescent 2′,7′-dichlorofluorescein (DCF). Briefly, after irradiation treatment, the medium was removed and replaced with a solution of 10 μM H_2DCF-DA in colorless DMEM (FluoroBrite™ DMEM, Gibco®, Waltham, MA, USA) and cells were incubated at 37 °C for 30 min. Then, the medium was aspirated and replaced with colorless DMEM. DCF fluorescence was measured using a Varioskan Lux multimode microplate reader (Thermo Fisher Scientific, Waltham, MA, USA) at 492 nm excitation and 517 nm emission.

TEM (transmission electron microscopy) cell images

After treatment, cells were first washed twice with phosphate-buffered saline (PBS, pH 7.4) and fixed in 2.5% glutaraldehyde prepared in 0.1 M sodium cacodylate buffer (pH 7.2) for 2 h at room temperature. Fixation was carried out in covered vials to prevent evaporation and preserve the ultrastructure. After fixation, the samples were rinsed three times (5 min each) in the same buffer to remove excess fixative.

Post-fixation was performed in 1% osmium tetroxide in 0.1 M sodium cacodylate buffer for 1 h at room temperature in the dark. The samples were then rinsed three times with distilled water (5 min each) to remove osmium residues.

Dehydration was achieved through a graded ethanol series: 30% (10 min), 50% (10 min), 70% (15 min), 90% (10 min), and two changes of 100% ethanol (10 min each). The samples were then transferred to propylene oxide (two changes, 10 min each) to facilitate resin infiltration.

Embedding was performed by gradual infiltration with a mixture of Epon resin and propylene oxide at increasing resin concentrations (1 : 3, 1 : 1, and 3 : 1, 1 h each step), followed by overnight infiltration in 100% resin. Samples were then placed in embedding moulds and polymerized at 60 °C for 48 h.

Ultrathin sections (70–90 nm) were cut using a diamond knife on an ultramicrotome (*e.g.*, Leica EM UC7) and collected onto 200-mesh copper grids. Sections were contrasted with 2% aqueous uranyl acetate for 10 min, rinsed with distilled water, and subsequently stained with lead citrate (Reynolds' method) for 3 min, followed by thorough washing with distilled water to prevent carbonate contamination.

Grids were examined in a transmission electron microscope (*e.g.*, JEOL JEM-1400) operating at 80 kV. Images were captured with a digital CCD camera and processed using the manufacturer's software.

Cell studies using magnetic hyperthermia

Magnetic hyperthermia (MH)-induced cytotoxicity was evaluated in human prostate cancer (PC3) and normal prostate epithelial (RWPE-1) cells using all nanoplatforms. All experiments were conducted using an optimized nanoparticle concentration of 20 μg Fe per mL, under an AFM of 16 kA m^{-1} and a frequency of 140 kHz for 30 minutes.

Author contributions

Beatriz Morais (B. M.): investigation, methodology, formal analysis, and writing the original draft; Vital Filho (V. F.): formal analysis, investigation, validation, and writing the original draft; Célia T. Sousa (C. T. S): conceptualization, investigation, formal analysis, methodology, validation, and writing the original draft; Fernanda Marques (F. M.): conceptualization, investigation, methodology, formal analysis, validation, and writing the original draft; Sara Lacerda (S. L.): conceptualization, investigation, methodology, formal analysis, validation, and writing the original draft; J. C. Waerenborgh (J. C. W.): conceptualization, investigation, methodology, validation, and writing the original draft; Bruno J. C. Vieira (B. J. C. V.): investigation and formal analysis; Teresa Pinheiro (T. P.): investigation, formal analysis, writing, and review; Rodica Mihaela Dinica (R. M. D.): methodology and validation; Maria J. Carmezim (M. J. C.): methodology and validation; Pedro M. P. Santos (P. M. P. S.): investigation, formal analysis, and methodology; Sandra Même (S. M.): investigation and formal analysis; Dirk H. Ortgies (D. H. O.): investigation and formal analysis; Laura C. J. Pereira (L. C. J. P.): conceptualization, formal analysis, methodology, validation, funding acquisition, project administration, writing the original draft, writing, review & editing, and supervision; Maria Paula Cabral Campello (M. P. C. C.): conceptualization, formal analysis, methodology, validation, funding acquisition, project administration, writing the original draft, writing, review & editing, and supervision.

Conflicts of interest

There are no conflicts to declare.

Data availability

The data are available within the article and supplementary information (SI). Supplementary information is available. The Supplementary Material contains: Table S1. Content of Fe, Au and Gd in the SPIONs, measured by PIXE (dry weight); Figure S1 – UV-vis spectra of nanoplatforms leaf extract SPLV, in Milli-Q water; Figure S2 – FTIR spectra for both routes of multifunctional nanoplatforms leaf extract SPLV; Figure S3 – Powder X-Ray diffraction patterns of (b) SP-LV-Au3-Gd and (d) SP-LV-Au1-Gd.; Figure S4 – Transmission electron microscopy images of (Up) SP-LV-Au3-Gd and (down) SP-LV-Au1-Gd, and respective histogram.; Figure S5 – Histograms of the size distribution by number of LV samples by DLS analysis.; Figure S6 – Histograms of the Zeta Potential distribution samples by DLS analysis; Figure S7 – Selection of the appropriate concentrations for the irradiation studies; *Radiosensitising studies by 60Co γ-rays* Figure S8 - t-test APA presented as mean ± SD (n = 4) with statistical significance represented as; $P < 0.12$, ns; $P < 0.033$, *; $P < 0.002$, **; $P < 0.001$, *** and Einstein Equation. See DOI: https://doi.org/10.1039/d6nr00113k.

Acknowledgements

This work was partially supported by the Fundação para a Ciência e a Tecnologia, FCT, I.P, through contracts with Centro de Ciências e Tecnologias Nucleares: UID/04349/2025 (https://doi.org/10.54499/UID/04349/2025), LTHMFL-NECL LIS-BOA-01-0145-FEDER-022096, UIDP/04565/2025 (iBB/IST) and LA/P/0140/2020 (Associate Laboratory Institute for Health and Bioeconomy – i4HB), the International Atomic Energy Agency (IAEA) Coordinated Research, CRP F11024-Research contract no. 26800, and PhD doctoral grant to VFF (PRT/BD/154845/2023). The authors gratefully acknowledge the assistance of the Instituto Gulbenkian de Ciência – Electron Microscopy Facility for TEM analyses. DHO is grateful for a Ramón y Cajal Fellowship Grant RYC2022-036732-I funded by MCIN/AEI/10.13039/501100011033 and by "ESF investing in your future". CTS acknowledges the program Atraccion de Talento (CAM), ref. 2020-T1/IND-19889 and the project PID2022-141080OB-C21. SL gratefully acknowledges Csilla Noémi Tóth for ICP measurements and the MRI sub-platform of the MO2VING facility (Orléans, France). FM gratefully acknowledges Dr António P. Matos from Centro de Investigação Interdisciplinar Egas Moniz (Caparica, Portugal) for fruitful discussion on TEM studies.

References

1 Y. Q. Meng, Y. N. Shi, Y. P. Zhu, Y. Q. Liu, L. W. Gu, D. D. Liu, A. Ma, F. Xia, Q. Y. Guo, C. C. Xu, J. Z. Zhang, C. Qiu and J. G. Wanget, *J. Nanobiotechnol.*, 2024, **22**, 24.
2 S. Faisal and O. Aboushoushah, *J. Sci.: Adv. Mater. Devices*, 2025, **10**(2), 100875.
3 A. Shakeri-Zadeh and J. W. M. Bulte, *Nat. Rev. Bioeng.*, 2025, **3**(3), 245–260.
4 E. Russell, V. Dunne, B. Russell, M. M. Ghita, S. J. McMahon, K. T. Butterworth, G. Schettino, C. K. McGarry and K. M. Prise, *Radiat. Oncol.*, 2021, **16**, 104.
5 D. Rivera, A. Bouras, M. Mattioli, M. Anastasiadou, A. C. Pacentra, O. Pelcher, C. Koziel, A. J. Schupper, T. Chanenchuk, H. Carlton, R. Ivkov and C. G. Hadjipanayis, *Sci. Rep.*, 2025, **15**, 10532.
6 C. Janko, T. Ratschker, K. Nguyen, L. Zschiesche, R. Tietze, S. Lyer and C. Alexiou, *Front. Oncol.*, 2019, **9**, 59.
7 X. Liu, Y. Zhang, Y. Wang, W. Zhu, G. Li, X. Ma, Y. Zhang, S. Chen, S. Tiwari, K. Shi, S. Zhang, H. M. Fan, Y. X. Zhao and X. J. Liang, *Theranostics*, 2020, **10**(8), 3793–3815.
8 Y. F. Zhang and M. Lu, *Front. Bioeng. Biotechnol.*, 2024, **12**, 1432189.
9 R. Lapusan, R. Borlan and M. Focsan, *Nanoscale Adv.*, 2024, **6**, 2234–2259.
10 M. Ruzycka-Ayoush, K. Sobczak and I. P. Grudzinski, *Toxicol. in Vitro*, 2024, **95**, 105760.
11 Y. Chen and S. Hou, *Cell Death Discovery*, 2023, **9**(1), 195.
12 V. C. Ferreira-Filho, B. Morais, B. J. C. Vieira, J. C. Waerenborgh, M. J. Carmezim, C. N. Tóth, S. Même, S. Lacerda, D. Jaque, C. T. Sousa, M. P. C. Campello and L. C. J. Pereira, *Molecules*, 2024, **29**(8), 1824.
13 H. Gu, S. Fu, Z. Cai and H. Ai, *J. Polym. Sci.*, 2024, **62**, 3103–3121.
14 R. Ghazi, T. K. Ibrahim, J. A. Nasir, S. Gai, G. Ali, I. Boukhris and Z. Rehman, *RSC Adv.*, 2025, **15**, 11587–11616.
15 J. Pellico, J. Ruiz-Cabello and F. Herranz, *ACS Appl. Nano Mater.*, 2023, **6**(22), 20523–20538.
16 H. Unterweger, L. Dézsi, J. Matuszak, C. Janko, M. Poettler, J. Jordan, T. Bäuerle, J. Szebeni, T. Fey, A. R. Boccaccini, C. Alexiou and I. Cicha, *Int. J. Nanomed.*, 2018, **3**(1), 1899–1915.
17 C. F. G. C. Geraldes, *Molecules*, 2024, **29**(6), 1352.
18 M. Yusefi, K. Shameli, O. Y. Su, S. Y. Teow, Z. Hedayatnasab, H. Jahangirian, T. J. Webster and K. Kuča, *Int. J. Nanomed.*, 2021, **16**, 2515–2532.
19 T. N. Aslan and Ü. Ünüvar, *Microchem. J.*, 2025, **2013**, 113643.
20 B. A. Eldeeb, W. M. A. El-Raheem and S. Elbeltagi, *Sci. Rep.*, 2023, **13**, 19000.
21 V. Krishanan, B. Devasena, M. Swetha, S. Priya and C. Geetha, *Bioscan*, 2025, **20**(2), 618–620.
22 A. A. M. Saeed, E. M. A. Mohsen and A. R. A. Bin Yahia, *Green Chem. Lett. Rev.*, 2025, **18**(1), 2525090.
23 B. Muzzi, M. Albino, A. Gabbani, A. Omelyanchik, E. Kozenkova, M. Petrecca, C. Innocenti, E. Balica, A. Lavacchi, F. Scavone, C. Anceschi, G. Petrucci, A. Ibarra, A. Laurenzana, F. Pineider, V. Rodionova and C. Sangregorio, *ACS Appl. Mater. Interfaces*, 2022, **14**(25), 29087–29098.
24 C. Caro, F. Gámez, P. Quaresma, J. M. Páez-Muñoz, A. Domínguez, J. R. Pearson, M. Pernía Leal, A. M. Beltrán, Y. Fernandez-Afonso, J. M. De la Fuente, R. Franco, E. Pereira and M. L. García-Martín, *Pharmaceutics*, 2021, **13**, 416.
25 A. Amraee, Z. Alamzadeh, R. Irajirad, A. Sarikhani, H. Ghaznavi, H. G. Harvani, S. R. Mahdavi, S. Shirvalilou and S. Khoei, *Cancer Nanotechnol.*, 2023, **14**, 61.
26 X. Ding, D. Li and J. Jiang, *Theranostics*, 2020, **10**(18), 8061–8079.
27 D. Levine, R. J. McDonald and H. Y. Kressel, *JAMA, J. Am. Med. Assoc.*, 2018, **320**(18), 1853–1854.
28 J. L. Domingo and R. C. Semelka, *Arch. Toxicol.*, 2025, **99**, 3897–3916.

29 M. Cudalbeanu, I. O. Ghinea, B. Furdui, D. Dah-Nouvlessounon, R. Raclea, T. Costache, I. E. Cucolea, F. Urlan and R. M. Dinica, *Molecules*, 2018, **23**, 1247.

30 T. T. Vicente, S. Arsalani, M. S. Quiel, G. S. P. Fernandes, K. R. Silva, S. Y. Fukada, A. J. Gualdi, É.J Guidelli, O. Baffa, A. A. O. Carneiro, A. P. Ramos and T. Z. Pavan, *Pharmaceutics*, 2024, **16**, 1474.

31 L. L. G. Al-mahamad, *Plasmonics*, 2025, **20**, 6565–6570.

32 F. Silva, A. Paulo, A. Pallier, S. Même, E. Tóth, L. Gano, F. Marques, C. F. G. C. Geraldes, M. M. C. A. Castro, A. M. Cardoso, A. S. Jurado, P. López-Larrubia, S. Lacerda and M. P. C. Campello, *Materials*, 2020, **13**(3), 513.

33 M. Cudalbeanu, D. Peitinho, F. Silva, R. Marques, T. Pinheiro, A. C. Ferreira, F. Marques, A. Paulo, C. F. Soeiro, S. A. Sousa, J. H. Leitão, A. Tăbăcaru, A. M. Avramescu, R. M. Dinica and M. P. C. Campello, *Nanomaterials*, 2021, **11**, 1562.

34 X. E. Mabasa, L. M. Mathomu, N. E. Madala, E. M. Musie and M. T. Sigidi, *Biochem Res Int.*, 2021, **28**, 2854217.

35 M. Yusefi, K. Shameli, R. R. Ali, S.-W. Pang and S.-Y. Teow, *J. Mol. Struct.*, 2020, **1204**, 127539.

36 H. Danafar, Y. Baghdadch, M. Barsbay, M. Ghaffarlou, N. Mousazadeh and A. Mohammadi, *Heliyon*, 2023, **9**(3), 13874A.

37 N. T. N. Linh, N. H. Du, N. T. Dung, L. T. T. Tam, P. H. Nam, P. T. H. Tuyet, L. T. Lu and L. T. Tam, *ChemistryOpen*, 2025, **14**, e202500166.

38 T. Girardet, S. Diliberto, C. Carteret, F. Cleymand and S. Fleutot, *Solid State Sci.*, 2023, **143**, 107258.

39 T. Strączek, S. Fiejdasz, D. Rybicki, K. Goc, J. Przewoźnik, W. Mazur, M. Nowakowska, S. Zapotoczny, S. Rumian and C. Kapusta, *Materials*, 2019, **12**, 1793.

40 D. Zahn, J. Landers, J. Buchwald, M. Diegel, S. Salamon, R. Müller, M. Köhler, G. Ecke, H. Wende and S. Dutz, *Nanomaterials*, 2022, **12**, 343.

41 S. O. Aisida, K. Ugwu, P. Akpa, A. C. Nwanya, U. Nwankwo, A. K. H. Bashir, I. Madiba, I. Ahmed and F. Ezema, *Mater. Today: Proc.*, 2021, **36**, 214–218.

42 R. Stein, B. Friedrich, M. Mühlberger, N. Cebulla, E. Schreiber, R. Tietze, I. Cicha, C. Alexiou, S. Dutz, A. R. Boccaccini and H. Unterweger, *Molecules*, 2020, **25**, 4425.

43 A. N. Dizaji, M. Yilmaz and E. Piskin, *Artif. Cells, Nanomed., Biotechnol.*, 2015, **44**(4), 1109–1115.

44 E. Nassireslami and M. Ajdarzade, *Adv. Pharm. Bull.*, 2018, **8**, 201–209.

45 A. Einstein, *Ann. Phys.*, 1905, **322**, 549–560.

46 A. Baer, S. E. Wawra, K. Bielmeier, M. J. Uttinger, D. M. Smith, W. Peukert, J. Walter and A.-S. Smith, *Small*, 2024, **20**, 2304670.

47 S. K. Filippov, R. Khusnutdinov, A. Murmiliuk, W. Inam, L. Y. Zrova, H. Zhang and V. V. Khutoryanskiy, *Mater. Horiz.*, 2023, **10**(12), 5354–5370.

48 N. Farkas and J. A. Kramar, *J. Nanopart. Res.*, 2021, **23**(5), 120.

49 T. Girardet, E. Bianchi, C. Henrionnet, A. Pinzano, S. Bouguet-Bonnet, C. Boulogne, S. Leclerc, F. Cleymand and S. Fleutot, *Mater. Today Commun.*, 2023, **36**, 106819.

50 H. S. N. Jayawardena, S. H. Liyanage, K. Rathnayake, U. Patel and M. Yan, *Anal. Chem.*, 2021, **93**(4), 1889–1911.

51 E. Murad, *Hyperfine Interact.*, 1998, **117**, 39–70.

52 A. G. Roca, J. F. Marco, M. D. P. Morales and C. J. Serna, *J. Phys. Chem.*, 2007, **C 111**, 18577–18584.

53 R. E. Vandenberghe, C. A. Barrero, G. M. Da Costa, E. Van San and E. De Grave, *Hyperfine Interact.*, 2000, **126**, 247–259.

54 A. G. Kolhatkar, A. C. Jamison, D. Litvinov, R. C. Willson and T. R. Lee, *Int. J. Mol. Sci.*, 2013, **14**, 15977–16009.

55 B. J. Sarkar and A. Bandyopadhyay, *J. Mater. Sci.: Mater. Electron.*, 2021, **32**, 1491–1505.

56 K. M. Kirkpatrick, B. H. Zhou, P. C. Bunting and J. D. Rinehart, *Chem. Sci.*, 2023, **14**, 7589.

57 A. Akbarzadeh, M. Samiei and S. Davaran, *Nanoscale Res. Lett.*, 2012, **7**, 144.

58 A. S. Saraiva, I. A. C. Ribeiro, M. H. Fernandes, A. C. Cerdeira, B. J. C. Vieira, J. C. Waerenborgh, L. C. J. Pereira, R. Cláudio, M. J. Carmezim, P. Gomes, L. M. Gonçalves, C. F. Santos and A. F. Bettencourt, *Int. J. Pharm.*, 2021, **593**, 120097.

59 R. V. Ramanujan, in *Biomedical Materials*, ed. R. Narayan, Springer New York, NY, USA, 2009, ch.17.

60 I. M. Obaidat, B. Issa and Y. Haik, *Nanomaterials*, 2015, **5**, 63–89.

61 A. Rajan, M. Sharma and N. K. Sahu, *Sci. Rep.*, 2020, **10**, 15045.

62 J. C. Matos, M. C. Gonçalves, L. C. J. Pereira, B. J. C. Vieira and J. C. Waerenborgh, *Nanomaterials*, 2019, **9**, 943.

63 Z. Shaterabadi, G. Nabiyouni, G. F. Goya and M. Soleymani, *Appl. Phys. A*, 2022, **128**, 631.

64 S. M. Dadfar, K. Roemhild, N. I. Drude, S. von Stillfried, R. Knüchel, F. Kiessling and T. Lammers, *Adv. Drug Delivery Rev.*, 2019, **138**, 302–325.

65 M. Unni, A. M. Uhl, S. Savliwala, B. H. Savitzky, R. Dhavalikar, N. Garraud, D. P. Arnold, L. F. Kourkoutis, J. S. Andrew and C. Rinaldi, *ACS Nano*, 2017, **11**, 2284–2303.

66 E. Tóth, L. Helm and A. Merbach, in *The Chemistry of Contrast Agents in Medical Magnetic Resonance Imaging*, ed. A. Merbach, L. Helm and É. Tóth, John Wiley & Sons, 2013, ch. 2, pp. 25–81.

67 B. Blasiak, F. C. J. M. van Veggel and B. Tomanek, *J. Nanomater.*, 2013, **2013**, 148578, 12 pages.

68 R. J. Holbrook, N. Rammohan, M. W. Rotz, K. W. MacRenaris, A. T. Preslar and T. J. Meade, *Nano Lett.*, 2016, **16**, 3202–3209.

69 K. Cheng, M. Yang, R. Zhang, C. Qin, X. Su and Z. Chen, *ACS Nano*, 2014, **8**, 9884–9896.

70 M. F. Ferreira, J. Gonçalves, B. Mousavi, M. I. M. Prata, S. P. J. Rodrigues, D. Calle, P. López-Larrubia, S. Cerdan, T. B. Rodrigues, P. M. Ferreira, L. Helm, J. A. Martinand and C. F. G. C. Geraldes, *Dalton Trans.*, 2015, **44**, 4016–4031.

71 F. J. Nicholls, M. W. Rotz, H. Ghuman, K. W. MacRenaris, T. J. Meade and M. Modo, *Biomaterials*, 2016, **77**, 291–306.

72 W. Zhang, J. A. Peters, F. Mayer, L. Helm and K. Djanashvili, *J. Phys. Chem. C*, 2015, **119**, 5080.

73 G. E. P. Box and H. L. Lucas, *Biometrika*, 1959, **46**, 77–90.

74 B. Mehdaoui, A. Meffre, J. Carrey, S. Lachaize, L.-M. Lacroix, M. Gougeon, B. Chaudret and M. Respaud, *Adv. Funct. Mater.*, 2011, **21**, 4573–4581.

75 H. Kahil, A. Faramawy, H. El-Sayed and A. Abdel-Sattar, *Crystals*, 2021, **11**(10), 1153.

76 K. P. Hazarika, C. Borgohain and J. P. Borah, *ACS Omega*, 2024, **9**(6), 6696–6708.

77 V.-K. Nguyen, S. W. Tsai, I. C. Cho, T. C. Chao, I. T. Hsiao, H. C. Huang and J. W. Liaw, *Nanomaterials*, 2025, **15**(4), 317.

78 T. Vangijzegem, V. Lecomte, I. Ternad, L. Van Leuven, R. N. Muller, D. Stanicki and S. Laurent, *Pharmaceutics*, 2023, **15**, 236.

79 Q. Song, Y. Zhang, X. Deng, H. Zhao, Y. Zhang, J. Li, W. Chen, H. Hu and Y. Zhang, *J. Mater. Chem. B*, 2023, **11**, 3836–3850.

80 M. J. Molaei, *J. Biomater. Appl.*, 2024, **39**(1), 3–23.

81 L. Chen, C. Chen, W. Pingping and S. Tao, *J. Nanomater.*, 2017, 1564634.

82 X.-S. Ke, Y. Ning, J. Tang, J.-Y. Hu, H.-Y. Yin, G. Wang, Z.-S. Yang, J. Jie, K. Liu, Z.-S. Meng, Z. Zhang, H. Su, C. Shu and J.-L. Zhang, *Chem. – Eur. J.*, 2016, **22**, 9676–9686.

83 F. Silva, A. Zambre, M. P. C. Campello, L. Gano, I. Santos, A. M. Ferraria, M. J. Ferreira, A. Singh, A. Upendran, A. Paulo and R. Kannan, *Bioconjugate Chem.*, 2016, **27**, 1153–1164.

84 A. N. Dizaji, M. Yilmaz and E. Piskin, *Artif. Cells, Nanomed., Biotechnol.*, 2015, **44**(4), 1109–1115.

85 A. Barge, G. Cravotto, E. Gianolio and F. Fedeli, *Contrast Media Mol. Imaging*, 2006, **1**(5), 184–188.

86 V. Uvarov and I. Popov, *Mater. Charact.*, 2013, **85**, 111–123.

87 R. Hergt and S. Dutz, Magnetic particle hyperthermia—biophysical limitations of a visionary tumour therapy, *J. Magn. Magn. Mater.*, 2007, **311**, 187–192.

88 D. Kouzoudis, G. Samourgkanidis, A. Kolokithas-Ntoukas, G. Zoppellaro and K. Spiliotopoulos, *Front. Mater.*, 2021, **8**, 638019.

89 S. C. Freitas, J. H. Belo, A. Granja, M. Canhota, A. S. Silva, S. Reis, H. Crespo, J. P. Araújo and C. T. Sousa, *Adv. Mater. Interfaces*, 2023, **10**, 220.

90 X. Chen, Z. Zhong, Z. Xu, L. Chen and Y. Wang, *Free Radical Res.*, 2010, **44**(6), 587–604.